Monthly Notices
of the
ROYAL ASTRONOMICAL SOCIETY

MNRAS **515,** 167–184 (2022)
Advance Access publication 2022 June 25

https://doi.org/10.1093/mnras/stac1737

Cluster assembly and the origin of mass segregation in the STARFORGE simulations

Dávid Guszejnov [1★] Carleen Markey [1,2,3] Stella S. R. Offner [1] Michael Y. Grudić [4] Claude-André Faucher-Giguère [4] Anna L. Rosen [5] and Philip F. Hopkins [6]

[1]*Department of Astronomy, University of Texas at Austin, TX 78712, USA*
[2]*Department of Physics and Astronomy, Purdue University, 525 Northwestern Avenue, West Lafayette, IN 47907, USA*
[3]*Department of Physics | Carnegie Mellon University, 5000 Forbes Avenue, Pittsburgh, PA 15213, USA*
[4]*CIERA and Department of Physics and Astronomy, Northwestern University, 2145 Sheridan Road, Evanston, IL 60208, USA*
[5]*Center for Astrophysics | Harvard & Smithsonian, 60 Garden St, Cambridge, MA 02138, USA*
[6]*TAPIR, California Institute of Technology, Mailcode 350-17, Pasadena, CA 91125, USA*

Accepted 2022 June 14. Received 2022 May 19; in original form 2022 January 6

ABSTRACT

Stars form in dense, clustered environments, where feedback from newly formed stars eventually ejects the gas, terminating star formation and leaving behind one or more star clusters. Using the STARFORGE simulations, it is possible to simulate this process in its entirety within a molecular cloud, while explicitly evolving the gas radiation and magnetic fields and following the formation of individual, low-mass stars. We find that individual star-formation sites merge to form ever larger structures, while still accreting gas. Thus clusters are assembled through a series of mergers. During the cluster assembly process, a small fraction of stars are ejected from their clusters; we find no significant difference between the mass distribution of the ejected stellar population and that of stars inside clusters. The star-formation sites that are the building blocks of clusters start out mass segregated with one or a few massive stars at their centre. As they merge the newly formed clusters maintain this feature, causing them to have mass-segregated substructures without themselves being centrally condensed. The merged clusters relax to a centrally condensed mass-segregated configuration through dynamical interactions between their members, but this process does not finish before feedback expels the remaining gas from the cluster. In the simulated runs, the gas-free clusters then become unbound and breakup. We find that turbulent driving and a periodic cloud geometry can significantly reduce clustering and prevent gas expulsion. Meanwhile, the initial surface density and level of turbulence have little qualitative effect on cluster evolution, despite the significantly different star formation histories.

Key words: stars: formation – stars: kinematics and dynamics – stars: luminosity function, mass function – galaxies: star clusters: general.

1 INTRODUCTION

Stars predominantly form in dense clusters of hundreds to a few 10^5 stars (Lada & Lada 2003; Bressert et al. 2010), making cluster formation a key part of the star formation process. Newly formed clusters can dissolve due to gas ejection resulting from stellar feedback, internal relaxation, dynamical friction, and tidal fields (Krumholz, McKee & Bland-Hawthorn 2019), making the present day observable clusters the surviving members of the original population. Observed bound clusters have historically been categorized as *open clusters* and *globular clusters* depending on their location and age, but emerging evidence suggests that these two classes are not different with regards to their formation and internal dynamics but instead experience a different cosmological history (see e.g. Kruijssen 2014 and the review of Krumholz et al. 2019). Unbound clusters are often referred to as stellar associations and are typically found at sites of recent star formation (Gouliermis 2018).

The relatively low number of observed clusters compared to the abundance of star formation sites suggests that most (non-massive) star formation sites create only short-lived clusters (Lada & Lada 2003). Longer-lived bound clusters must require specific star formation histories and initial conditions (see Krumholz & McKee 2020 for details). The exact formation mechanism of clusters within star-forming molecular clouds is not known, despite intense theoretical and observational effort. However, recent observations (e.g. Bressert et al. 2010; Gouliermis 2018) support the idea of hierarchical star formation, where stars form in regions of various densities, prescribed by the underlying hierarchy of ISM structure (e.g. along filaments). Simulations of small star-forming clouds have reproduced this scenario and formed-bound star clusters through hierarchical assembly, where small sub-clusters merge with their neighbours, eventually forming a massive bound structure (e.g. Bonnell, Bate & Vine 2003; Vázquez-Semadeni, González-Samaniego & Colín 2017; Grudić et al. 2018).

A key step in the cluster formation process is the onset of stellar feedback that first stops the accretion of individual stars then expels the gas from the cluster. Exactly how this gas expulsion happens has

★ E-mail: guszejnov.david@gmail.com

dramatic effects on the future evolution of the cloud (Krause et al. 2020). Violent gas expulsion leads to the quick dissolution of the cluster (i.e. 'infant mortality', see Hills 1980; Lada & Lada 2003; Baumgardt & Kroupa 2007; Fall, Krumholz & Matzner 2010), however highly substructured clusters may survive even instantaneous gas expulsion (Farias et al. 2018). Recent hydrodynamical simulations have also found indications of gravitational feedback from gas expulsion (Geen et al. 2018; Zamora-Avilés et al. 2019), such that asymmetry in the expelled gas shell produces a net gravitational force on the stars. *Gaia* measurements have identified several clusters undergoing gas expulsion, which appear to be expanding (Kuhn et al. 2019).

The stellar distribution also provides insights into the initial conditions and past cluster evolution. Many observed star clusters exhibit mass segregation, whereby massive stars are concentrated in the centres of clusters (Hillenbrand & Hartmann 1998; Kirk & Myers 2011). Mass segregation may be a natural outcome of the star formation process, such that clusters are born segregated (e.g. McKee & Tan 2003; Bonnell & Bate 2006). In this scenario massive stars form at the locations with the highest density gas, such that mass segregation is primordial. Alternatively, star clusters may not be initially non-segregated but become so due to dynamical interactions (Spitzer 1969) that cause massive stars to sink to the bottom of the potential well, i.e. the cluster centre. Numerical investigations have been limited by the dynamic range of star formation simulations as the simulation must track the formation of individual stars and model their motions over the cluster relaxation time-scale. Thus, works investigating the origin of mass segregation have been constrained to modelling small clusters (e.g. Kirk, Offner & Redmond 2014) and clusters without self-consistent gas treatment (e.g. Parker 2014).

In this paper, we present radiation magneto-hydrodynamic (RMHD) simulations from the STAR FORmation in Gaseous Environments (STARFORGE) project.[1] These simulations follow the evolution of turbulent and magnetized giant molecular clouds (GMCs) from the onset of star formation until it is disrupted by stellar feedback, while also following the formation of individual stars above the H burning limit (for details see Grudić et al. 2021a and Guszejnov et al. 2021, henceforth referred to as Paper I and Paper II). Note that the hydrodynamic simulations previously used to study star cluster formation in the literature had smaller dynamic ranges, so they were either restricted to simulating a small clump (e.g. Kirk et al. 2014) or did not follow individual low-mass stars (e.g. Geen et al. 2018; Zamora-Avilés et al. 2019). The STARFORGE simulations follow the the assembly of star clusters through gas dispersal, which is modelled self-consistently by including all major feedback processes (i.e. protostellar jets, stellar radiation and winds, supernovae). This allows us to determine whether mass segregation is primordial and explore the role mergers play in cluster assembly. Note that in this work we focus on the stellar clustering in the simulations. For a detailed analysis on the cloud evolution, star formation history, and stellar mass spectrum, see the companion paper Grudić et al. (2022) (henceforth referred to as Paper II)

We briefly summarize the STARFORGE simulations in Section 2.1, and refer the reader to Paper I for more details on the numerical capabilities of STARFORGE. Our cluster identification methods are detailed in Section 2.2 with special attention to the time dependent nature of the cluster assignment problem. We present our results for the fiducial cloud parameter simulation in Section 3, describing the evolution of cluster properties in Section 3.2, mass segregation in Section 3.3, and the mass function of stellar populations inside and outside clusters in Section 3.4. In Section 4, we investigate how variations in the initial cloud conditions, including the initial surface density, velocity dispersion, geometry, and turbulent driving affect the cluster formation process. We discuss the implications of these results and the related caveats in Section 5. Finally, we summarize our results and conclusions in Section 6.

2 NUMERICAL METHODS

2.1 The STARFORGE simulations

For this work we utilize simulations from the STARFORGE project, which are run with the GIZMO code.[2] A full description and presentation of the STARFORGE methods including a variety of tests and algorithm details are given in Paper I. We only briefly summarize the key points here. Readers familiar with the STARFORGE simulation methods should skip ahead to Section 2.2.

2.1.1 Physics

We simulate star-forming clouds with the GIZMO code (Hopkins 2015), using the Lagrangian meshless finite-mass (MFM) method for magnetohydrodynamics (Hopkins & Raives 2016), assuming ideal MHD (with the constrained gradient scheme of Hopkins 2016 to ensure that $\nabla \cdot \mathbf{B} = 0$ to high numerical precision.

Gravity is solved with an improved version of the Barnes–Hut tree method from Springel (2005) with high-order integration of sink particle trajectories to accurately follow multiple sink systems. Force softening is fully adaptive for gas cells (Price & Monaghan 2007; Hopkins 2015). Accreting sink particles (stars) have a fixed 18 AU kernel radius. We adopt the sink formation and accretion algorithm from Bate, Bonnell & Price (1995), while accurately accounting for thermal, magnetic, kinetic and gravitational energies, and angular momentum. As such we are able to follow the formation and evolution of binaries and multiples with separations larger than the softening length.

Sink particles represent individual stars. Once they form they follow the protostellar evolution model from Offner et al. (2009a), which is also used in the ORION code.

In this model, the protostar is treated as a collapsing polytrope: The collapse is divided into distinct phases during which the qualitative behaviour changes. These phases are 'pre-collapse', 'no burning', 'core deuterium burning at fixed temperature', 'core deuterium burning at variable temperature', 'shell deuterium burning', and 'zero age main sequence'. This module dynamically evolves stellar properties (e.g. radius, accretion, and internal luminosities) throughout the simulation. For details see Appendix B of Offner et al. (2009a) and Paper I.

'Non-isothermal' or 'cooling' STARFORGE runs utilize the radiative cooling and thermo-chemistry module presented in Hopkins et al. (2018) that contains detailed metallicity-dependent cooling and heating physics from $T = 10$–10^{10} K, including recombination, thermal bremsstrahlung, metal lines (following Wiersma, Schaye & Smith 2009), molecular lines, fine structure (following Ferland et al. 2013), and dust collisional processes. The cooling module self-consistently solves for the internal energy and ionization state of the gas (see Appendix B of Hopkins et al. 2018). The gas adiabatic index is calculated from a fit to density based on the results of Vaidya

[1] http://www.starforge.space

[2] http://www.tapir.caltech.edu/~phopkins/Site/GIZMO.html

et al. (2015). The runs in this paper explicitly treat radiation (RHD runs), unlike Paper II. This means co-evolving the gas, dust, and radiation temperature self-consistently as in Hopkins et al. (2020), including the stellar luminosity in various bands accounting for photon transport, absorption, and emission using dust opacity. We use a first-moment or M1 (Levermore 1984) RHD solver with a reduced-speed-of-light (RSOL) of 30 km s^{-1} and transport photons in five distinct bands (IR, optical/NIR, NUV, FUV, and ionizing). Our treatment automatically handles the trapping of cooling radiation in the optically-thick limit. In addition to local sources (i.e. stars) an external heating source is added representing the interstellar radiation field (ISRF) and a temperature floor of $T_{\rm floor} = 2.7$ K (corresponding to the cosmic microwave background temperature) is enforced.

As shown in Paper II, protostellar jets represent a crucial feedback mechanism as they dramatically reduce stellar masses that is achieved not just by launching some of the accreted material, but also by perturbing the accretion flow around the star. We model their effects by having sink particles launch a fixed fraction of the accreted material along their rotational axis with the Keplerian velocity at the protostellar radius. See Paper I for details on the numerical implementation.

In addition to their radiative feedback, massive main-sequence stars inject a significant amount of mass, energy, and momentum into their surroundings through stellar winds. We calculate the mass-loss rates based on a prescription given in Grudić et al. (2021a), motivated by Smith (2014), and wind velocities per Lamers, Snow & Lindholm (1995). Winds are implemented either through local mass, momentum, and energy injection or direct gas cell spawning, depending on whether the free-expansion radius can be resolved. To account for Wolf–Rayet (WR) stars that dominate the wind energy and momentum budget we use a simple prescription where the mass loss rate of $M > 20\,{\rm M}_\odot$ stars is increased at the end of their lifetime using the WR lifetime prescription of Meynet & Maeder (2005).

Finally, massive stars end their life as a supernova (SN). In the simulation, all $> 8\,{\rm M}_\odot$ stars are eligible to become a supernova at the end of their lifetime, for which the minimum is set as 3 Myr. SNe lead to an isotropic ejection of all mass with a total energy of $E_{\rm SN} = 10^{44}\,{\rm J} = 10^{51}$ erg, which is implemented through direct gas cell spawning.

The simulations in this paper include all of the physical processes detailed above.

2.1.2 *Initial conditions & parameters of clouds*

We generate our initial conditions (ICs) using MakeCloud (Grudic & Guszejnov 2021), identical to Paper II. Unless otherwise specified, our runs utilize 'Sphere' ICs, meaning that we initialize a spherical cloud (radius $R_{\rm cloud}$ and mass M_0) with uniform density, surrounded by diffuse gas with a density contrast of 1000. The cloud is placed at the centre of a periodic $10R_{\rm cloud}$ box. The initial velocity field is a Gaussian random field with power spectrum $E_k \propto k^{-2}$ (Ostriker, Stone & Gammie 2001) compromised of a natural mixture of compressive and solenoidal modes, scaled to the value prescribed by the $\alpha_{\rm turb} \equiv 5\sigma^2 R_{\rm cloud}/(3GM_0)$ turbulent virial parameter where σ is the 3D gas velocity dispersion. The initial clouds have a uniform B_z magnetic field whose strength is set by the μ, normalized mass-to-flux ratio (Mouschovias & Spitzer 1976). There is no external driving in these simulations. Note that the initial temperature is effectively set by the gas-dust mixture quickly reaching equilibrium with the interstellar radiation field (ISRF), for which we assume solar neighbourhood conditions (Draine 2011).

We also run simulations using 'Box' ICs, similar to the driven boxes used in e.g. Li et al. (2004), Federrath et al. (2014a), Cunningham et al. (2018). These are initialized as a constant density, zero velocity periodic cubic box with the same temperature prescription as 'Sphere' ICs. This periodic box is then 'stirred' using the driving algorithm by Federrath et al. 2010; Bauer & Springel 2012. This involves a spectrum of $E_k \propto k^{-2}$ of driving modes in Fourier space at wavelengths 1/2–1 the box size, with an appropriate decay time for driving mode correlations ($t_{\rm decay} \sim t_{\rm cross}$). This stirring is initially performed without gravity for five global freefall times $\left(t_{\rm ff} \equiv \sqrt{\frac{3\pi}{32G\rho_0}}\right)$, to achieve saturated MHD turbulence. The normalization of the driving spectrum is set so that in equilibrium the gas in the box has a turbulent velocity dispersion that gives the desired $\mathcal{M}$ and $\alpha_{\rm turb}$, same as in the Sphere runs. We use purely solenoidal driving, which remains active throughout the simulation after gravity is switched on. We take the box side-length $L_{\rm box}$ to give a box of equal volume to the associated Sphere cloud model. An important difference between the Sphere and Box runs is that in the case of driven boxes the magnetic field is enhanced by a turbulent dynamo (Federrath et al. 2014b) and saturates at about $\alpha_{\rm B} \sim 0.1$ (i.e. 10 per cent relative magnetic energy to gravitational, see Guszejnov et al. 2020), so for Box runs the 'pre-stirring' magnetic field strength (defined by μ) does not directly specify the actual initial magnetic field strength when gravity is turned on (however the 'pre-stirring' flux in the box will still affect the large-scale geometry of the magnetic field).

Table 1 shows the target parameters for the runs we present in this paper. The input parameters are the cloud mass M_0, size R_0, turbulent virial parameter $\alpha_{\rm turb}$, and normalized magnetic mass-to-flux ratio μ (note that initial temperature is set by the ISRF). Similar to Paper II, we set-up our clouds to lie along a mass-size relation similar to observe GMCs in the Milky Way (e.g. Larson 1981; Lada & Dame 2020, specifically assuming $\Sigma \equiv M_0/\pi R_{\rm cloud}^2 = 63\,{\rm M}_\odot\,{\rm pc}^{-2}$), except for our one model with 10x higher surface density. These clouds are marginally bound ($\alpha_{\rm turb} = 2$, except for variation models) and start out in thermal equilibrium with the ISRF. For the initial magnetization, we assume $-E_{\rm mag}/E_{\rm grav} = 0.01$, which translates to $\mu = 4.2$. The initial gas metallicity is assumed to be equal to the solar value. The STARFORGE simulations we use have a mass resolution of $\Delta m = 10^{-3}\,{\rm M}_\odot$, making the mass function incomplete for brown dwarfs ($M < 0.08\,{\rm M}_\odot$), which are thus omitted from our analysis (see Paper I for convergence tests). For Sphere runs, the simulations are run until stellar feedback quenches star formation and subsequently disrupts the cloud (see Fig. 1). In case of the Box runs, the periodic boundary conditions trap both radiation and cloud material, so the run is terminated when the box becomes saturated by stellar radiation.

2.2 Cluster identification

Despite almost a century of study, there is no one who accepted the definition of what a star cluster is, as the 'classical' picture of an isolated, bound, centralized group of stars is not applicable to most observations (Krumholz et al. 2019). Previous work in the literature defined star clusters using an absolute density threshold (Lada & Lada 2003), relative density contrast (McKee, Parravano & Hollenbach 2015), boundedness (Portegies Zwart, McMillan & Gieles 2010), Bayesian decomposition into ellipsoids (Kuhn et al. 2014), and numerous other techniques (see Schmeja 2011 for examples). Due to the lack of consensus in the literature, we choose a cluster definition that is both simple and robust for time series data (see

Table 1. Simulations used in this paper described with STARFORGE label conventions. *Top:* Physics modules included, see Section 2.1.1 and Paper I for details on the individual physics modules. *Bottom:* Initial conditions of clouds used in our runs, with M_0, $R_{\rm cloud}$, $\alpha_{\rm turb}$, and μ being the initial cloud mass, size, virial parameter, mass to magnetic flux ratio respectively (note that in runs that explicitly evolve RHD the initial gas-dust temperature is set by the ISRF). We also report the initial 3D turbulent velocity dispersion σ, thermal virial parameter $\alpha_{\rm th}$, total virial parameter α, Alfvén Mach number $\mathcal{M}_{\rm A}$, plasma β, magnetic virial parameter $\alpha_{\rm B}$, as well as the relative Jeans, sonic and magnetic mass scales (see section 2 in Guszejnov et al. 2020 for definitions). Note that the parameters in this table apply to both Box and Sphere runs as they are set up to have identical initial global parameters, with $L_{\rm box}$ being the box size for Box runs and $R_{\rm cloud}$ being the cloud radius for Sphere runs. Note that Box runs have slightly different initial parameters (e.g. Mach number, virial parameter) due to the non-exact scaling of the driving, so the values shown here are the target values.

Physics label	Thermodynamics	MHD	Protostellar Jets	Stellar Radiation	Stellar Winds & SNe												
C_M_J_RT_W	Non-isothermal, RHD (C)	Ideal (M)	Included (J)	Included (RT)	Included (W)												
			Input Parameters				**Derived Parameters**									**Resolution**	
Cloud label	M_0 [$M_\odot$]	$R_{\rm cloud}$ [pc]	$L_{\rm box}$ [pc]	$\alpha_{\rm turb}$	μ	σ [km/s]	$\alpha_{\rm th}$	α	$\mathcal{M}_{\rm A}$	β	$\alpha_{\rm B}$	$\frac{M_{\rm Jeans}}{M_0}$	$\frac{M_{\rm sonic}}{M_0}$	$\frac{M_\Phi}{M_0}$	$M_0/\Delta m$	$\Delta x_{\rm J}$ [AU]
M2e4	2×10^4	10	16	2	4.2	3.2	0.008	2.03	10	0.78	0.02	3×10^{-3}	7×10^{-5}	0.1	2×10^7	30
M2e4_R3	2×10^4	3	–	2	4.2	5.8	0.008	2.02	10	0.23	0.02	5×10^{-4}	7×10^{-6}	0.1	2×10^7	30
M2e4_a1	2×10^4	10	–	1	4.2	2.3	0.008	1.03	10	0.78	0.02	3×10^{-3}	4×10^{-5}	0.1	2×10^7	30
M2e4_a4	2×10^4	10	–	4	4.2	4.5	0.008	4.03	10	0.78	0.02	3×10^{-3}	1×10^{-4}	0.1	2×10^7	30

Section 2.2.1). We identify star clusters using the DBSCAN (Density-based spatial clustering of applications with noise, Ester et al. 1996) clustering algorithm from the scikit-learn PYTHON library (Pedregosa et al. 2011), similar to Wall et al. (2020). DBSCAN assigns group membership using the following algorithm:

(i) Any star above the H burning limit ($> 0.08\,{\rm M}_\odot$) whose $N_{\rm min}$ closest neighbours are within λ distance is considered a 'core particle'.

(ii) All connected core particles and any particles within λ distance are considered to be part of the same cluster. Particles not assigned to clusters are considered to be 'noise.'

We apply DBSCAN to the 3D spatial positions of the stars, and we adopt $N_{\rm min} = 10$ and $\lambda = 1$ pc, which effectively serves as our cluster definition. We find that changing $N_{\rm min}$ has no qualitative effects on our results. Reducing $\lambda = 1$ pc reduces the size and mass of newly formed clusters, increases the overall number of clusters and delays mergers, however we find the evolution of cluster properties for the largest clusters to be similar.

Note that we also experimented with other, more advanced clustering methods that do not require a specified spatial scale, e.g. HDBSCAN (McInnes, Healy & Astels 2017). Algorithms like HDBSCAN identify the clustering scales from the data, thus providing results that are not biased by the somewhat arbitrary choice of clustering scale in DBSCAN. While HDBSCAN has been successfully applied to observed young clusters (Kerr et al. 2021), we find that it can create confusing cluster assignments if applied to time-series data. This is because the definition of what counts as a cluster in HDBSCAN is determined by the current configuration of stars, which can lead to the algorithm non-physically splitting up and merging clusters between different snapshots of a simulation. We also experiment with applying the clustering algorithm to the full 6D phase space data instead of only the 3D spatial positions, similar to the procedure applied to observational data. Doing so, however, requires a mapping from velocity to spatial scales (i.e. a phase-space metric, see Behroozi, Wechsler & Wu 2013 for an example). After experimenting with several different methods (e.g. assume a linewidth-size relation, 'pre-cluster' in 3D and find velocity dispersion within clusters), we ultimately find no clear advantage to using velocity data, as their main role in observations is to filter out 'interloper' field stars, which are not present in our simulations.

2.2.1 *Cluster tracking*

This work aims to follow the formation and evolution of clusters, which creates a unique challenge that observations do not face, namely that cluster assignments and evolution need to be meaningful and continuous over multiple snapshots. To address this issue, we apply a series of cleaning operations after the initial cluster assignments, according to the following algorithm:

(i) Assign initial cluster memberships for stars in each independent snapshot using DBSCAN.

(ii) Identify clusters persisting through multiple snapshots. For each cluster X in snapshot i we follow the steps:

(a) Find all clusters Y in snapshot $i-1$ for which X contains at least half of the stars of Y. From these the one that contains the largest fraction of stars from X is considered to be the past version of X.

(b) If no such cluster Y exists we look over older snapshots ($<i-1$, going backwards in time) and look for a cluster Y

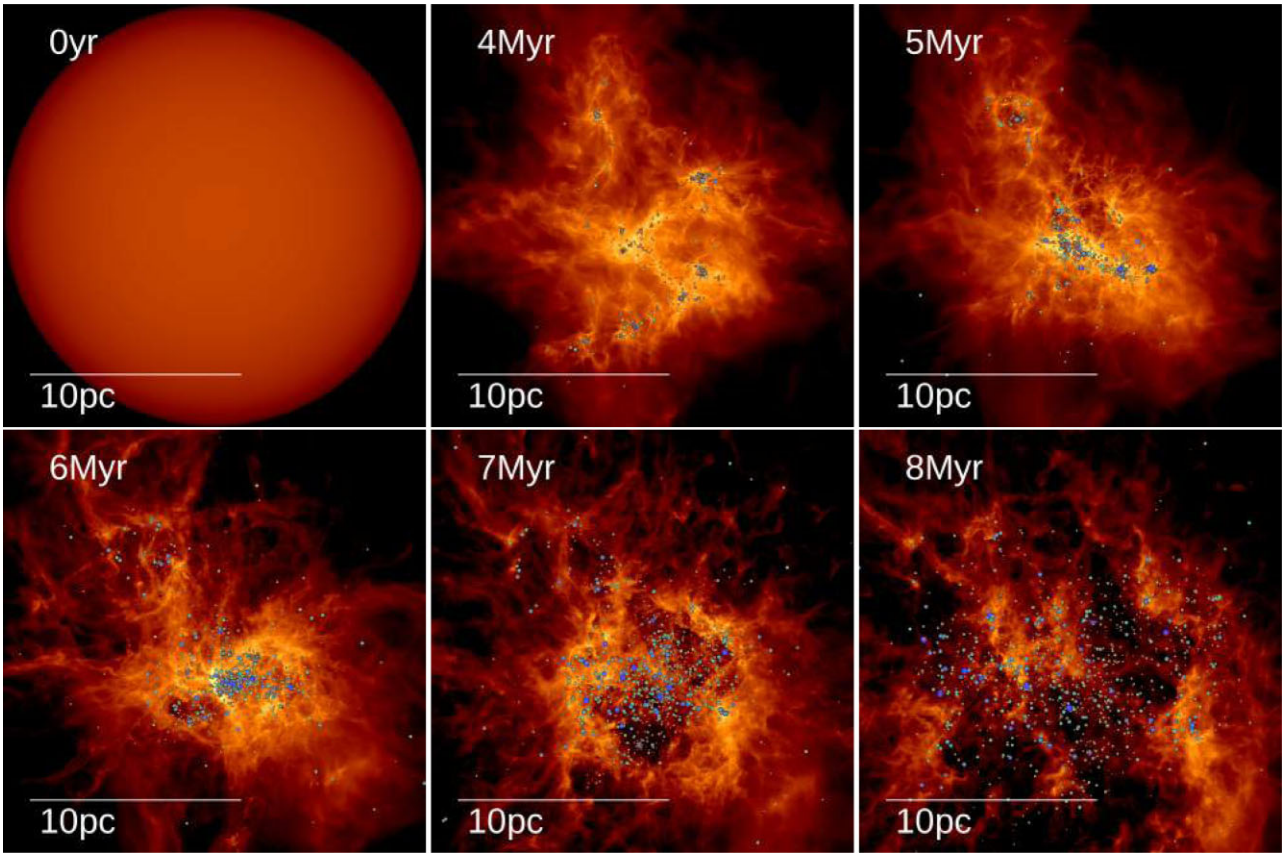

Figure 1. Surface density maps for **M2e4_C_M_J_RT_W** (our fiducial run), which is an $M_0 = 2 \times 10^4\,\mathrm{M}_\odot$ mass cloud resolved with $M_0/\Delta m = 2 \times 10^7$ initial gas cells (see Table 1), at different times, from the beginning of the simulation until cloud disruption. The colour scale is logarithmic and the circles represent sink particles (stars) that form in high-density regions where fragmentation can no longer be resolved. The size of the circles is increasing with mass as well as their colour changing from red ($M \sim 0.1\,\mathrm{M}_\odot$), through green ($M \sim 1\,\mathrm{M}_\odot$) to blue ($M \sim 10\,\mathrm{M}_\odot$). This simulation resolves a dynamic range from $\sim$20 pc down $\sim$30 AU and is run until stellar feedback quenches star formation and disrupts the cloud.

where X and Y mutually contain at least half of the stars of the other, and consider that to be the past version of X.

(c) If no past version was identified we declare cluster X to be a newly-formed cluster.

(iii) Create a 'cluster label history' for each star and then apply the following cleaning operations with a characteristic time-scale of $t_{\rm clean} = 100\,\mathrm{kyr}$, which effectively sets a lower limit for the cluster lifetime:

(a) Remove short-lived ($<t_{\rm clean}$) clusters. If their stars belonged to another (not short-lived) cluster directly before joining this cluster, they keep their original assignment. This fixes a problem that arises when the clustering algorithm temporarily splits part of a cluster and then merges it back after a few snapshots. Note that short-lived cluster splits are rare when using DBSCAN and such clusters contain only a small fraction of the stars, but removing them is necessary to reduce non-physical discontinuities in the properties of larger clusters.

(b) Inspect each star's cluster membership history and remove intermittent label assignments. If a star that initially belongs to cluster X is assigned to cluster Y and then back to X within $t_{\rm clean}$ (i.e. Y in a sequence of X, X, Y, X, X), then all Y assignments are changed to X. This removes 'flip-flopping' cluster assignments. We then remove any assignments that last a very short time ($t_{\rm clean}/2$). This is similar to the previous operation, but does not take into account the final label (i.e. Y a sequence of X, X, Y, Z, Z). With these two steps we eliminate transient clusters and flip-flopping from ambiguous assignments during cluster mergers.

(iv) We repeat the second step and re-assign cluster IDs using the cleaned cluster label histories. This corrects errors during the original assignment, e.g. a large cluster temporarily splitting into several smaller ones.

2.3 Cluster properties and definitions

To describe the star clusters in our simulations we introduce several physical quantities. We define the cluster radius (also known as 'mean-square radius' or 'Spitzer radius', see Spitzer & Harm 1958), as

$$R^2 \equiv \langle ||\Delta \mathbf{x}||^2 \rangle, \tag{1}$$

where $\langle \dots \rangle$ denotes averaging over cluster members and $\Delta\mathbf{x}$ is the distance of a member star from the centre of mass of the cluster. We also define the *half-mass radius*, R_{50}, as the radius around the centre of mass that encloses half the cluster mass. We define the 3D cluster velocity dispersion as

$$\sigma_{\rm 3D}^2 \equiv \langle ||\Delta \mathbf{v}||^2 \rangle, \tag{2}$$

where $\Delta\mathbf{v}$ is the relative velocity of a member star to the centre of mass of the cluster.

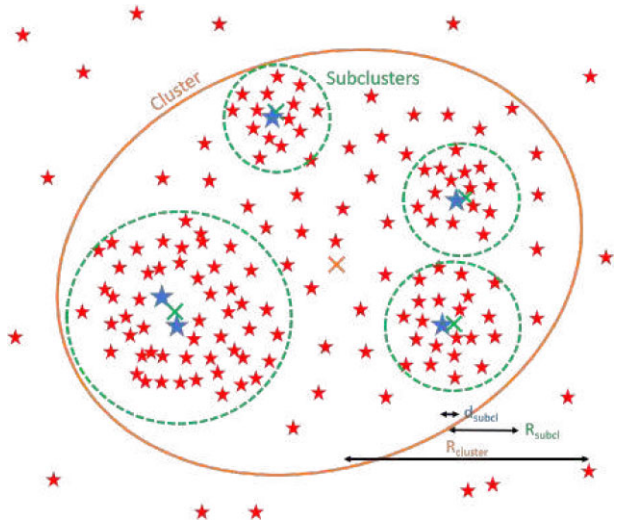

Figure 2. Cartoon illustration of a young cluster with mass segregated subclusters, where low and high-mass stars are marked as red and blue, respectively, showing also the centres of both the cluster and the subclusters denoted with cross markers. Due to the subclusters having only 1–2 massive stars, the mean edge length of the MST (equation 9) would yield $\Lambda_{MSR} \sim R_{cluster}/R_{cluster} = 1$, ignoring mass segregation on the subcluster level. Meanwhile, the mass segregation offset (see equation 10) would be $\Lambda_{MSO} \sim R_{subc}/d_{subc} \gg 1$.

To characterize the cluster boundedness we use the virial parameter

$$\alpha \equiv \frac{2E_{kin}}{-E_{grav}}, \tag{3}$$

where E_{kin} and E_{grav} are the total kinetic and gravitational binding energy of the stars within the cluster. Note that hard binaries are common, but naively including their binding energy when trying to determine the overall boundedness of the cluster (i.e. virial parameter) yields misleading results, as these binaries essentially interact with the rest of the cluster as if they were a single point particle.[3] Thus, it is instructive to define the system virial parameter where we merge binary and multiple systems (identified using the same algorithm as Bate 2009 and Guszejnov, Hopkins & Krumholz 2017)

$$\alpha_{sys} \equiv \frac{2E_{kin,sys}}{-E_{grav,sys}}. \tag{4}$$

Here, $E_{kin,\,sys}$ and $E_{grav,\,sys}$ are the total kinetic and gravitational binding energy of the cluster after we replaced binary/triple/quadruple systems with their centres of mass. We can similarly define a 3D system velocity dispersion within the cluster

$$\sigma^2_{3D,sys} \equiv \langle ||\Delta \mathbf{v}_{sys}||^2 \rangle_{sys}, \tag{5}$$

where $\langle \dots \rangle_{sys}$ is averaging over systems within the cluster. Note that close binaries are often unresolved in observed clusters, making the velocity dispersion inferred by observations closer to $\sigma^2_{3D,sys}$ than σ^2_{3D}.

Note that these definitions take neither gas cells nor sink particles outside the cluster into account. Considering that clusters inevitably form in areas with dense gas, the contribution of gas to the initial boundedness is significant. As a crude estimate we calculate the amount of gas within the spatial extent of the cluster (R from equation 1) and calculate its contribution to the gravitational energy of the cluster members ($E_{grav,\,gas}$) by assuming that this mass is distributed homogeneously within the cluster. This leads to the α' and α'_{sys} virial parameters:

$$\alpha' \equiv \frac{2E_{kin}}{-E_{grav} - E_{grav,gas}}, \tag{6}$$

$$\alpha'_{sys} \equiv \frac{2E_{kin,sys}}{-E_{grav,sys} - E_{grav,gas,sys}}. \tag{7}$$

Note that by definition $\alpha' \leq \alpha$, and it only becomes equal at later times when most of the gas has been expelled from the cluster. These estimates are within a factor of few of the values returned by directly calculating the contributions from gas within the cluster.

In our simulations we find that clusters tend to expand after gas expulsion. The clustering algorithm (Section 2.2) often breaks these expanding clusters into separate smaller clusters. In order to quantify the cluster expansion we introduce the mass-weighted mean radial velocity

$$\bar{v}_{rad} = \frac{\sum m v_{rad}}{\sum m}, \tag{8}$$

where v_{rad} is the radial velocity of a star relative to the cluster centre of mass and the summation is over all cluster members.

2.3.1 Mass segregation

Observed clusters exhibit mass segregation, i.e. massive stars are 'distributed differently' than lower mass stars (Krumholz et al. 2019). This often means that they are concentrated at the minimum of the gravitational potential, i.e. the dense centre of the cluster (Hillenbrand & Hartmann 1998). Many studies adopt this more specific criterion to define mass segregation. There are several methods in the literature to characterize this phenomenon relying on the cluster density profiles (e.g. Hillenbrand 1997) or characteristic radial distance (Gouliermis, de Grijs & Xin 2009) of stars in various mass bins. Alternatively, one can also calculate the slope of the mass function of stars at different radii from the cluster centre (de Grijs et al. 2002). These methods, however, are sensitive to the choice of mass bins and annuli (Gouliermis et al. 2004) and to the precise determination of the cluster centre. An alternative metric that is insensitive to these is to construct a minimum spanning tree (MST), the shortest graph connecting all stars without closed loops. Comparing the characteristic MST edge length between massive stars and randomly chosen stars can quantify the level of mass segregation in the cluster (see e.g. Cartwright & Whitworth 2004 and Allison et al. 2009).

In this work, we consider two separate mass segregation metrics for clusters. The first one is based on the definition of Allison et al. (2009), which quantifies the degree of mass segregation using the mass segregation ratio (MSR)

$$\Lambda_{MSR} \equiv \frac{\langle l_{norm} \rangle_{MC}}{l_{massive}}, \tag{9}$$

where $l_{massive}$ is the mean edge length of the MST between massive stars only. We define massive stars for the remainder of this paper as any star above $5\,M_\odot$. Meanwhile, l_{norm} is the mean edge length for $N_{massive}$ randomly chosen stars, where $N_{massive}$ is the number of massive stars. The $\langle \dots \rangle_{MC}$ operation denotes constructing $N_{sets} = 500$ random sets and averaging over them, so $\langle l_{norm} \rangle_{MC}$ is the mean of the median MST edge lengths from N_{sets} of random realizations. Since this metric is only meaningful if at least several massive stars exist, we require $N_{massive} \geq 5$ for it to be defined.

[3]Observational estimates of the virial parameter likely also suffer from biases introduced by binaries, see Gieles, Sana & Portegies Zwart (2010).

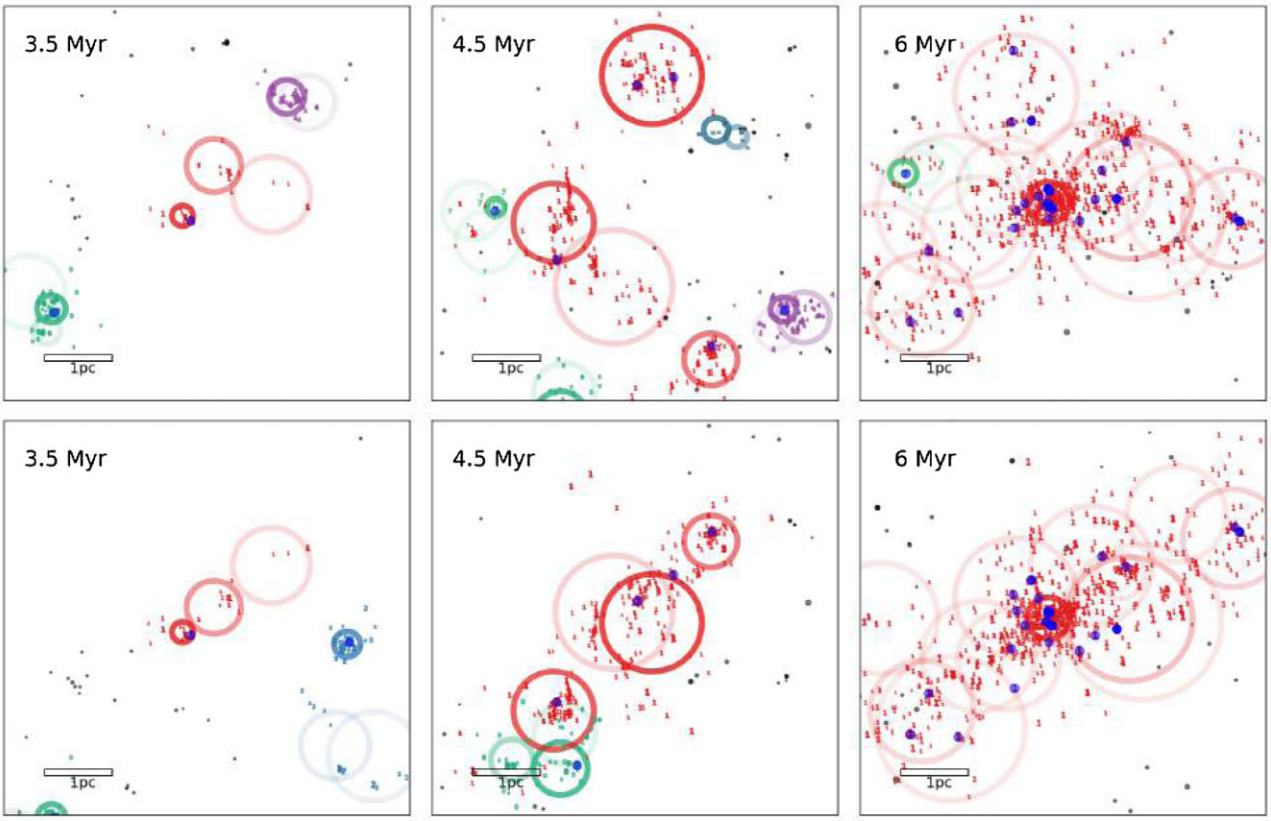

Figure 3. Cluster assignment of stars in the fiducial run (coloured according to Fig. 4), projected into the X-Y (*top row*) and X-Z (*bottom row*) planes. In addition, the position of massive stars ($> 5\,M_\odot$) are marked with semi-transparent blue circles (note that some of them are in tight binaries, which makes them appear as a single opaque circle). Subclusters identified by the variational Bayesian Gaussian mixture model (see Section 3.3 and Fig. 2) are highlighted by rings (opacity increasing with mass contained). Each star formation site only has a few massive stars (usually a single or a binary) that are in the centre. As these merge to form ever larger clusters, the centralized substructure remains until gas expulsion after which *N*-body dynamics relax the cluster into a centralized configuration.

A significant drawback of the MST based method is that it requires at least several massive stars to be already present in the cluster, while both observations (Kirk & Myers 2011) and simulations (Kirk et al. 2014) find that even small groupings of stars with a single massive star exhibit signs of mass segregation. We find that our clusters, like observed young clusters (Kirk & Myers 2011; Kerr et al. 2021), are initially highly structured, where the stellar distribution follows the hierarchical distribution of the star-forming gas. In this case, the MST method does not detect mass segregation as it only exists within smaller sub-groups of stars, i.e. if the cluster consists of several mass-segregated subclusters.

To address this issue we identify coherent groups of stars, subclusters, within each cluster. We define these subclusters as centrally condensed stellar over-densities and divide every cluster into one or more subclusters. We identify subclusters in each of our clusters by applying the variational Bayesian Gaussian mixture cluster identifying algorithm (Attias 2000; Bishop 2006) from the scikit-learn library, using the default parameters and setting the maximum number of components to $N_{\rm massive}$. This Gaussian mixture method decomposes the cluster into several Gaussian density distributions, which are, by our definition, subclusters (see Fig. 2 for a cartoon illustration and Fig. 3 for later examples from the simulations). Unlike the DBSCAN algorithm we use to identify the clusters themselves, Gaussian mixture models in general require no specific length-scale and the specific variational method can infer the appropriate number of Gaussian components, i.e. subclusters. Note that we do not use the variational Bayesian Gaussian mixture model to identify the clusters themselves in the simulations, because this method suffers from the same assignment persistence issues as other clustering algorithms without spatial scales (see Section 2.2).

In order to account for cluster substructure, we introduce a second metric for mass segregation, the mass segregation offset (MSO):

$$\Lambda_{\rm MSO} \equiv \left\langle \frac{d_{\rm subcl}}{R_{\rm subcl}} \right\rangle_{\rm all} \Bigg/ \left\langle \frac{d_{\rm subcl}}{R_{\rm subcl}} \right\rangle_{\rm massive}, \tag{10}$$

where $d_{\rm subcl}$ is the distance from a star to the centre of the nearest subcluster. For simplicity we disregard whether the star is a member of this nearest subcluster. $R_{\rm subcl}$ is the size scale of the subcluster (defined following equation 1), while the $\langle \ldots \rangle_{\rm massive}$ operation denotes averaging over all massive stars in the cluster (see Fig. 2). Note that in this definition, we introduce the concept of 'subcluster', which makes the definition of equation (10) in theory different from similar offset measures in the literature (Kirk et al. 2014), although it gives the same answer for small or highly centralized clusters.

Finally, we define the mass segregation time-scale for a star of mass M as (Spitzer 1969; Binney & Tremaine 1987):

$$t_{\rm seg}(M) = \frac{\langle m \rangle}{M} \frac{N}{8 \ln N} \frac{R}{\sigma_{\rm sys}}, \tag{11}$$

where $\langle m \rangle$ is the average stellar mass in the cluster, while N is the number of its members, R is the cluster size (equation 1) and $\sigma_{\rm sys}$ is its velocity dispersion. Note that using the system velocity dispersion changes the results by a factor of 2.

3 CLUSTER FORMATION AND EVOLUTION IN THE FIDUCIAL M2E4 RUN

In this section we detail the formation and evolution of clusters within our fiducial run (**M2e4**, Sphere) that are identified using the methodology described in Section 2.2.

3.1 General behaviour

We find that star formation begins at several locations in the cloud, which we refer to as star formation sites. These sites produce a few massive stars (often just a single one) as well as many lower mass stars, forming a small cluster (see Fig. 3). These small clusters are still gas-dominated, actively accreting, and star-forming when they encounter similar nearby clusters and merge with them, forming larger clusters, with these structures becoming subclusters in them. This behaviour is similar to previous results claiming hierarchical cluster assembly from similar initial conditions (e.g. Bonnell et al. 2003; Grudić et al. 2018). The newly formed clusters continue accreting gas and forming new stars, as well as merging with other structures until feedback from massive stars terminates star formation and expels the remaining gas (see Fig. 1).

Fig. 4 shows the formation and merger history of newly formed clusters depicting the hierarchical build-up of larger structures via mergers of smaller clusters. This leads to the formation of a 'dominant' cluster that ultimately encompasses most of the stellar mass in the simulation. Once stellar feedback expels the gas from a cluster, the remaining stars are not gravitationally bound and the cluster starts breaking into smaller structures. This mainly affects the largest cluster, which becomes unbound and expands, breaking up into many smaller clusters.

3.2 Cluster properties

To illustrate the evolution of cluster properties in our simulations we focus on the 'dominant' cluster that eventually encompasses the majority of stars at the end of the simulation. Fig. 5 shows the cluster properties defined in Section 2.3. The dominant cluster reaches about 1000 members and attains roughly $1000\,M_\odot$ by the time the cloud disrupts (see panels a-b), containing the majority of the total stellar mass. This run endes with SFE $= M_\star/M_0 \sim 7$ per cent, corresponding to $M_\star \sim 1400\,M_\odot$). Clusters form around individual star formation sites, and these structures merge to form larger objects, leading to 'jumps' in the cluster size. Although gravitational attraction between the various substructures and stellar interactions should shrink the cluster over time and increase the central stellar density (Krause et al. 2020), the continuous formation of new stars from infalling gas and mergers with other clusters causes the cluster to maintain its size until gas expulsion occurs (Fig. 5 panel c).

As the star cluster grows rapidly in both mass and size the velocity dispersion also increases (Fig. 5, panel d). Note that the stellar velocity dispersion, σ_{3D}, is super-virial due to the effect of close binaries. Meanwhile, the velocity dispersion for systems, $\sigma_{3D,\,sys}$, (equation 5) is fairly close to the virial value (if the gas potential is also taken into account). The stellar velocity dispersion peaks as the cluster reaches its maximum mass, just as gas expulsion starts. It declines subsequently as the cluster breaks apart. Thus, the statistics follow a shrinking fraction of the original cluster.

We expect that most close binaries are unresolved in observed clusters (e.g. Foster et al. 2015; Kerr et al. 2021), so the observationally inferred velocity dispersion should be close to $\sigma_{3D,\,sys}$. Thus, simple estimates using the global cluster mass and size scales

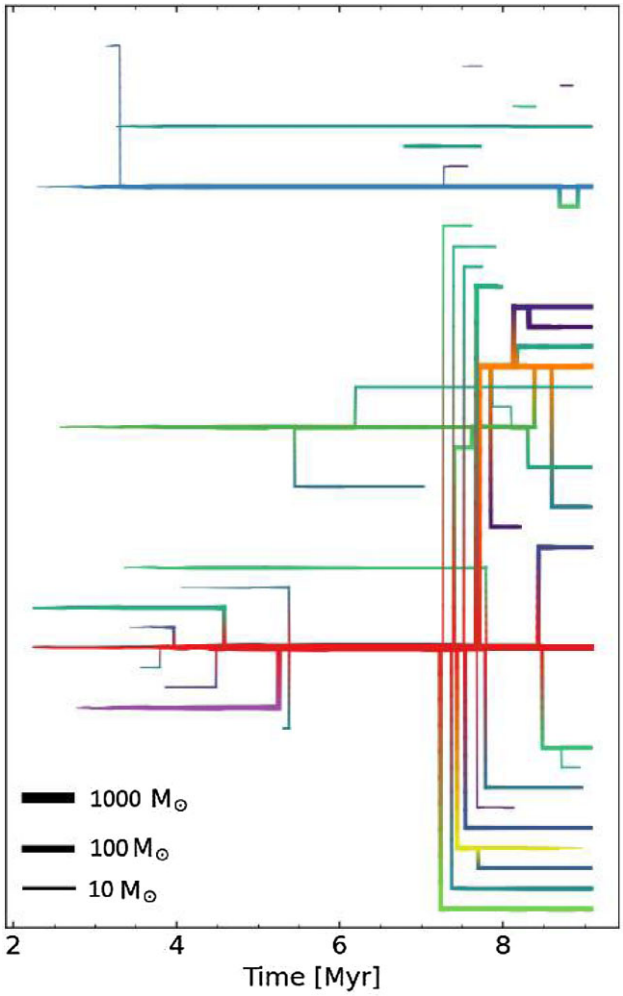

Figure 4. Merger history of clusters in the fiducial **M2e4** run. Each line represents a cluster (using its assigned colour) with a width that logarithmically increases with mass. Mergers and splits are denoted by connecting the lines at the time of the event. The line representing the cluster ends if the cluster dissolves. The initial behaviour is hierarchical assembly where clusters merge to form ever greater structures. This continues until feedback expels gas from the cluster, so it becomes unbound and begins to break into smaller clusters.

(after including the enclosed gas mass) would conclude these clusters are virialized during star formation (as in Foster et al. 2015) and highly supervirial during the breakup phase after star formation ceases and/or a significant fraction of the gas mass has been expelled. Meanwhile, direct calculation of the virial parameter using equation 3 indicates the cluster is highly sub-virial with $\alpha \sim 1/2$–1 (Fig. 5, panel e). We find that the gravitational potential energy is dominated by hard binaries, leading to low α values. After merging these systems, i.e. using the definition from equation 4), α_{sys} is consistently above the boundedness limit of $\alpha = 2$. However, initially the clusters are strongly gas-dominated, so after correcting for the gas potential (equation 7) we find the clusters are initially strongly bound ($\alpha' < 1$, similar to the results of Offner, Hansen & Krumholz 2009b) and then become unbound after gas expulsion ($\alpha' \sim 10$). The resulting unbound cluster immediately expands and breaks into smaller structures. Since the simulation stops shortly after gas expulsion, it is unclear what fraction of the original cluster will remain bound. This will be investigated in a future STARFORGE project.

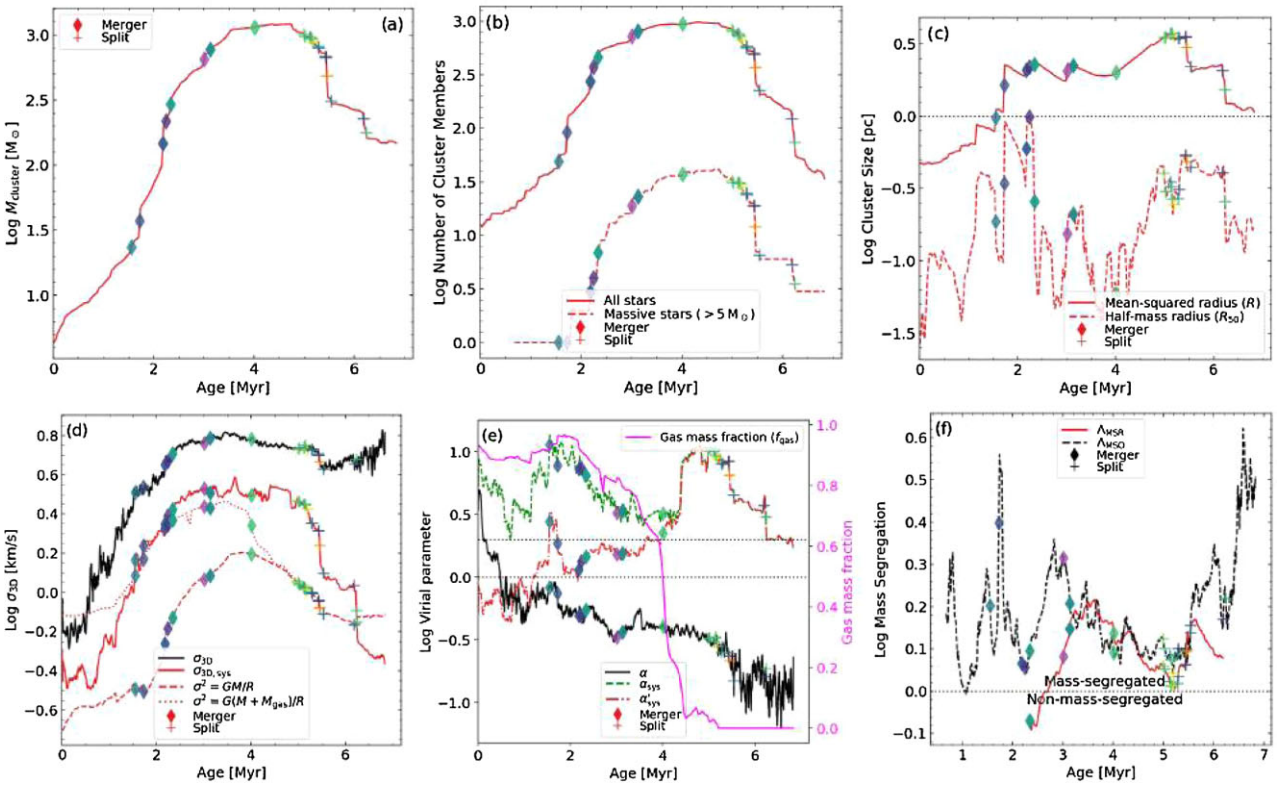

Figure 5. Evolution of the dominant cluster in the fiducial run (**M2e4**, Sphere), highlighting major events, i.e. mergers with another cluster (diamonds) and the splitting of the cluster (crosses), coloured according to Fig. 4. Dotted horizontal lines mark the characteristic scale of our cluster size definition (1 pc), the virial equilibrium and marginal boundedness ($\alpha = 1$ and 2) and the boundary between regular and inverse mass segregation. The top row shows the total stellar mass in the cluster (top left), number of cluster members (top middle), and the cluster size scales (top right, equation 1), respectively. The bottom row shows the cluster velocity dispersion (left, equation 2), virialization state (middle, equations 3–7), and mass segregation (right, equations 9–10). Note that all values are smoothed with a 30 kyr averaging window to make the plots easier to read. For an analysis of the main trends see Section 3.2.

Table 2. General cluster and sink properties of various runs (see Table 1), including the final star formation efficiency (SFE = $M_{*,\,\mathrm{final}}/M_{\mathrm{cloud}}$), relative mass of stars in clusters versus outside clusters (calculated as $\max(M_{\mathrm{in\,clusters}})/M_{*,\mathrm{final}}$) and the relative weight of the dominant cluster ($\max(M_{\mathrm{dominant\,cluster}})/\max(M_{\mathrm{in\,clusters}})$).

Label	SFE ($M_{*,\,\mathrm{final}}/M_{\mathrm{cloud}}$)	$\max(M_{\mathrm{in\,clusters}})/M_{*,\mathrm{final}}$	$\max(M_{\mathrm{dominant\,cluster}})/\max(M_{\mathrm{in\,clusters}})$
M2e4	8%	83%	94%
M2e4 Box, with driving	5%	45%	64%
M2e4 Box, no driving	9%	73%	46%
M2e4_a1	11%	80%	94%
M2e4_a4	4%	67%	79%
M2e4_R3	14%	87%	99%

3.3 Evolution of mass segregation

Fig. 5 shows that the dominant cluster develops mass segregation (panel f) according to both the Λ_{MSR} and Λ_{MSO} metrics (see equations 9–10). However, these metrics differ on the initial degree of mass segregation, with Λ_{MSO} identifying segregation from the time, the first massive stars form, while Λ_{MSR} only detecting it at much later times. In the early stage of cluster evolution, each cluster is composed of the stars formed in one to a few star formation site and hosts only a few massive stars in the centre (see Fig. 3), leading to a $\Lambda_{\mathrm{MSO}} > 1$ (at this stage they have <5 massive stars so Λ_{MSR} is not defined). These sites continue to accrete, form more stars, and merge with others, thereby forming ever-larger clusters. The resulting merged clusters inherit the centrally condensed substructures, thus maintaining $\Lambda_{\mathrm{MSO}} > 1$. Note that it is not the case for Λ_{MSR}, which drops at the start of mergers due to the initial distance between the subclusters dominating the MST edge lengths. Once the merger is underway, the subclusters interact and sink towards the centre, increasing Λ_{MSR}. Eventually, the cluster relaxes to a centrally condensed, 'classical' star cluster with $\Lambda_{\mathrm{MSO}} > 1$ and $\Lambda_{\mathrm{MSR}} > 1$. This redistribution occurs on a time-scale of $t_{\mathrm{seg}} \sim 2$ Myr for massive stars (see equation 11). Before the cluster can fully dynamically relax, stellar feedback expels the remaining gas and unbinds the cluster. Still, as gas expulsion begins, massive stars are already preferentially located near the centre of the dominant cluster, leading to high Λ_{MSR} and Λ_{MSO} values. During the gas dispersal process, massive stars that formerly reside near the centre move outwards with the rest of the cluster, causing both mass segregation metrics to drop. Note that at later times Λ_{MSO} may increase, but it is due to the cluster identification algorithm splitting the dominant cluster into smaller clusters, which tend to have a few massive stars at their centres.

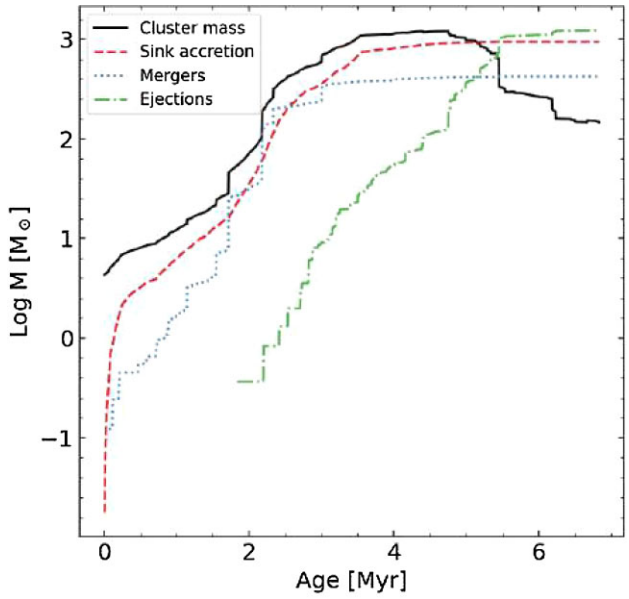

Figure 6. Mass history of the dominant cluster in the fiducial run (**M2e4**, Sphere). Lines show the current cluster mass (solid), cumulative mass the cluster acquired by stellar members, by accreting gas (dashed) and through cluster mergers (dotted). The total mass of stars ejected from the cluster is shown by the dash–dotted line. Over its lifetime the cluster gains most of its mass by accreting gas, while mergers and accretion contribute roughly equally to the cluster growth while there are clusters to merge with. Before gas expulsion (around 4.5 Myr, see Fig. 5) the cluster ejects roughly 10 per cent of its stellar mass.

3.4 Mass distribution of stars inside and outside clusters

We find that the majority of stars that form in our simulations end up in clusters, although a significant fraction (∼10 per cent) are ejected before gas expulsion (see Table 2 and Fig. 6). During its lifetime the dominant cluster in the fiducial simulation gains stellar mass from two sources: 1) mergers with other clusters and 2) gas accretion by its stellar members or newly formed stars within the cluster. We find these two mechanisms to have roughly similar weight during most of the cluster lifetime, with accretion becoming more important after most stars have merged with the dominant cluster, leaving no other clusters to merge with. After gas expulsion the cluster becomes unbound and loses an order unity of its mass.

Fig. 7 shows the mass distribution of various stellar populations in the fiducial simulation just as gas expulsion starts due to strong radiative feedback (around 4.5 Myr into the simulation). We find that about 80 per cent of stars are cluster members where more than 90 per cent of these belong to the dominant cluster. The mass distributions of the clustered and non-clustered stars are similar up to 10 $M_\odot$, but we can not rule out that the distribution deviate at the high-mass end. The distributions are statistically consistent with the Kroupa (2002) IMF fitting function except at very high masses, because the overall simulation IMF is slightly top-heavy (to be described in more detail in an upcoming paper). Fig. 7 further shows that the mass distribution for the dominant cluster is similar to that of the ejected stars (with a significance of $p = 0.96$ obtained from a two-sample Kolmogorov–Smirnov test). There is no indication of preferential ejection of more massive stars before gas expulsion. Unsurprisingly the stellar mass distributions of the dominant cluster and the full simulation are also similar.

4 EFFECTS OF INITIAL CONDITION VARIATIONS ON CLUSTERS

In this section we investigate the effects of turbulent driving (Section 4.1), the initial level of turbulence (Section 4.2) and surface density (Section 4.3) on the properties of the dominant cluster. These properties have a significant effect on the star formation history of the system, and here we examine the impact of these properties on clustering.

4.1 Cloud setup and turbulent driving (Box versus Sphere)

As noted in Section 2.1.2, the Sphere versus Box configurations have two important differences, which may lead to different clustering properties. First, the periodic boundary conditions of the Box set-up leads to both an order-of-magnitude shallower gravitational potential (Federrath & Klessen 2012) and prevents the escape of radiation and gas. Second, the Box setup starts from a self-consistent, pre-stirred state, and this external driving is continuous throughout the run, providing energy for turbulent modes on the box scale that cascade down to smaller scales. To disentangle the effects of these two factors,

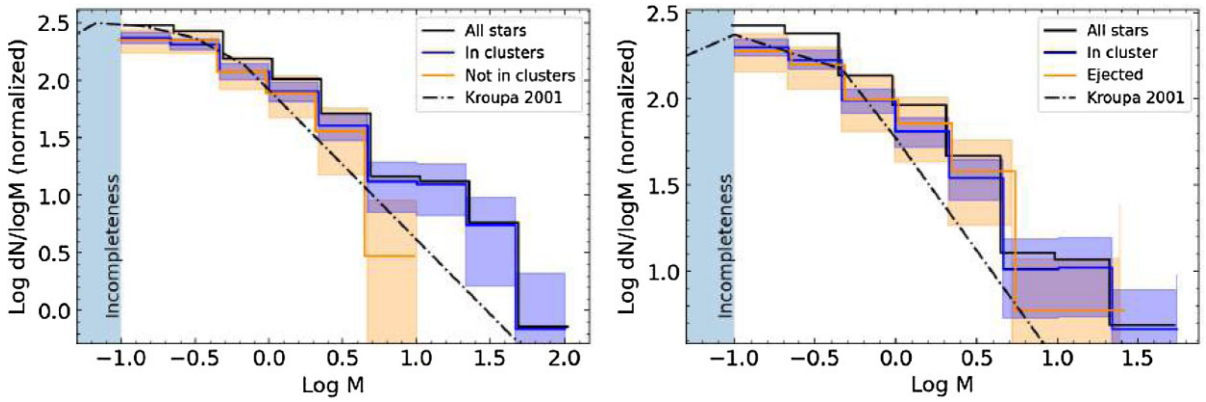

Figure 7. Left: Mass distribution of sink particles (stars), comparing three populations: those assigned to clusters (blue), those that are not assigned to clusters (orange), and the full stellar population (black). The spectrum is taken at the time when the dominant cluster reaches its maximum mass (i.e. just as gas expulsion starts). Shaded regions denote the two sigma Poisson uncertainties. We also show the Kroupa (2002) canonical fitting function for the MW IMF from the literature and mark the completeness limit of the simulation. Right: Similar to the left-hand panel, but concentrating on the dominant cluster only. We compare three populations: those assigned to the dominant cluster (blue), those that were ejected from it (orange) and the full stellar population (black).

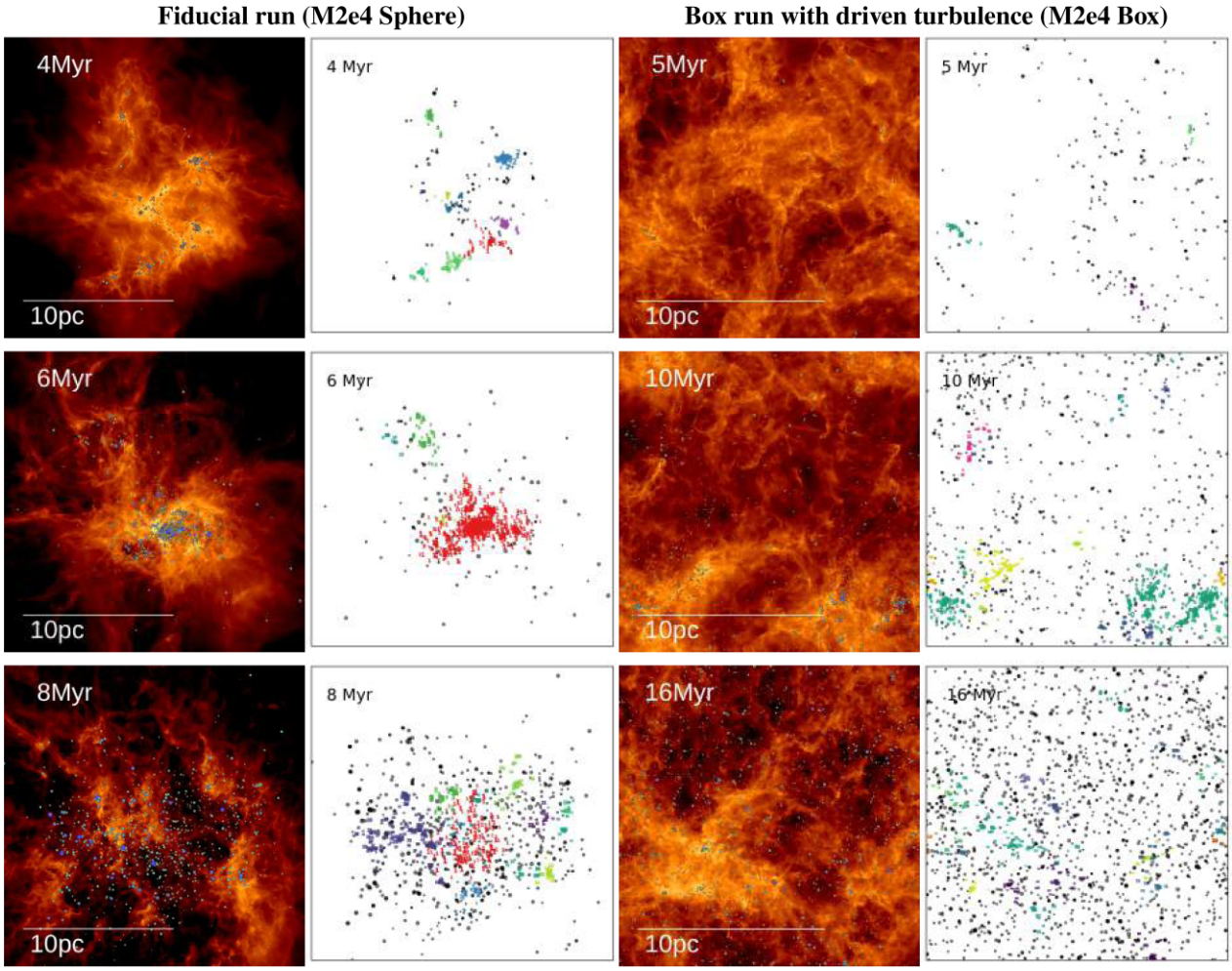

Figure 8. The surface density maps and cluster assignments of the **M2e4** runs with both 'Sphere' and 'Box' ICs. The surface density maps use the same conventions as Fig. 1. On the cluster assignment maps, each star is represented with its cluster ID and coloured with the colour assigned to the cluster, while stars not assigned to clusters are marked with black circles.

we compare three **M2e4** runs (Table 1): 1) our fiducial Sphere run, 2) a Box run with continuous external driving, and 3) a Box run where we turn-off the driving after the initial 'stirring' phase.

We find that both periodic boundary conditions and turbulent driving significantly affect cluster properties. As mentioned in Section 2.1.2, periodic boundaries prevent both material and radiation from escaping the cloud, thus these runs never experience gas ejection that may lead to cloud disruption.

Fig. 8 shows that while the evolution of the Sphere run is well described as the hierarchical assembly of one dominant cluster, this is not the case in the driven Box run. Turning off turbulent driving restores this behaviour, as the gas undergoes global gravitational collapse once the initial turbulence decays (see Fig. 9). Note that even without turbulent driving, the shallower gravitational potential of the Box run relative to the Sphere run leads to weaker gravitational focusing, delaying mergers (see Fig. 10). We also find that continued turbulent driving leads to the formation of a significant number of transient clusters that survive for a few 100 kyr before dissolving.

Turbulent driving dramatically slows down star formation in the cloud (SFE $\propto t^2$ versus SFE $\propto t^3$), while in the non-driven case star formation is only suppressed until the initial turbulent velocity field decays. This is due to the weaker gravitational potential in the Box runs (Federrath & Klessen 2012), which produces weaker gravitational focusing in addition to the external driving that prevents global gravitational collapse. This is apparent in Fig. 11 as the dominant cluster in both Box runs grow significantly slower than in the Sphere one. While the initial cluster masses are similar between the driven and decaying runs, the decaying run has (on average) more massive members due to the slightly less top heavy IMF in the Box runs. Unlike the Sphere run, the Box runs experience no cloud disruption, and stellar feedback is unable to permanently expel gas from the cluster before the gas in the simulation volume is heated to unphysical temperatures by radiation trapped by the periodic boundary condition. There is no permanent gas expulsion, the clusters themselves do not suddenly become unbound (like in the Sphere run). Their future evolution, however, is uncertain as we stop the simulation when it reaches the unphysical, radiation-filled regime.

4.2 Initial level of turbulence

In this section we vary the initial velocity dispersion to determine the impact of the cloud turbulence on clustering. We compare Sphere runs with $\alpha_{\rm turb}$ values of 1,2 and 4, which correspond to bound, marginally bound, and unbound clouds, respectively. We find that the final star formation efficiency decreases with increasing $\alpha_{\rm turb}$ (see Table 2). Fig. 12 shows that higher $\alpha_{\rm turb}$ also leads to less

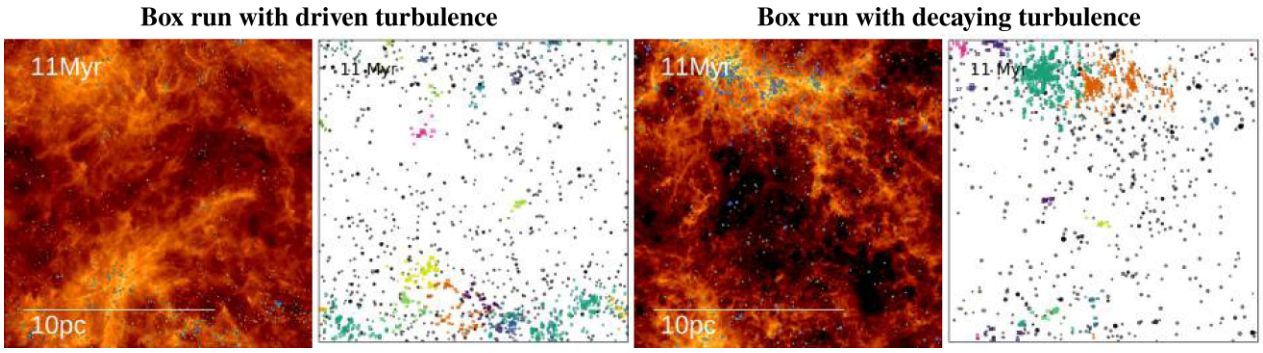

Figure 9. Same as Fig. 8 for **M2e4** Box runs with and without turbulent driving.

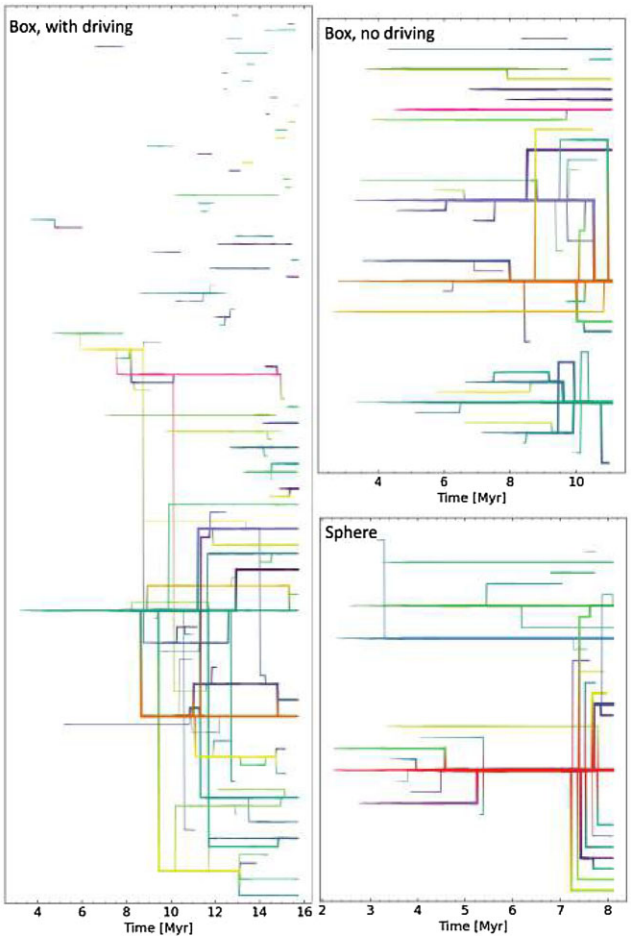

Figure 10. Merger histories for the **M2e4** Box runs with and without turbulent driving and the fiducial Sphere run, same as Fig. 4. Driving prevents the hierarchical merging of smaller clusters and leads to the formation of many transient clusters. The periodic boundary conditions of the Box run also reduce gravitational focusing relative to the Sphere run, suppressing mergers.

concentrated star formation and weaker global gravitational collapse due to increased turbulent support. However, the hierarchical cluster formation picture that we find for the fiducial run ($\alpha_{\rm turb} = 2$) still qualitatively applies (see Figs 8 and 12).

All runs produce a single dominant cluster. The final mass of this dominant cluster decreases with increased turbulence, mostly due to the lower final SFE values of the clouds (Table 2). Fig. 13 shows that the dominant cluster follows a qualitatively similar evolutionary trend in all runs, with higher masses and consequently higher velocity dispersions for runs with higher SFE (i.e. lower $\alpha_{\rm turb}$). The dominant cluster becomes unbound once stellar feedback expels the remaining gas, leading to its expansion, and breakup into smaller clusters. In Fig. 13, it appears as if the $\alpha_{\rm turb} = 4$ run had a much longer cluster lifetime. In fact, feedback causes the cluster to expel its gas content and become unbound in roughly the same time (4 Myr) as in the other cases (see gas mass fraction and $\alpha'_{\rm sys}$ panels of Fig. 13). At the same time the dominant cluster merges with two neighbouring clusters, increasing the effective size of the resulting cluster and the relative gas mass content.

We find that all three runs are mass-segregated from early times, and we see no clear trend in either $\Lambda_{\rm MSR}$ or $\Lambda_{\rm MSO}$ as a function of $\alpha_{\rm turb}$. Therefore, we conclude that mass segregation is not very sensitive to modest changes in the initial cloud virial parameter.

4.3 Surface density

Cloud surface density is thought to be a key parameter of star formation (Krumholz & McKee 2008; Fall, Krumholz & Matzner 2010; Grudić et al. 2021b) due to its influence on the dynamics of fragmentation and degree of stellar feedback. Although we present only one run with a different surface density (Sphere run with a factor 10 times increase in Σ; **M2e4_R3**), we also ran a calculation with 10 times lower surface density, but it had a final SFE value of only 1 per cent and produced no clusters with more than 20 stars, preventing a meaningful cluster analysis.

As expected, increasing the surface density leads to enhanced star formation and a higher final SFE (Table 2). Higher surface density also means that the cloud is smaller, making it easier for the clustering algorithm (see Section 2.2) to join star formation sites. Consequently, nearly all stars end up in one massive cluster (Fig. 14). Similar to the fiducial run, the dominant cluster is gas-dominated and becomes unbound once stellar feedback expels the gas. The characteristic time-scale of cloud evolution is the freefall time, which, due to the higher overall density, is significantly shorter than that of our fiducial run (Fig. 15). Note that the cluster assembly phase is mainly determined by this time-scale, while the length of the following gas expulsion phase depends on both the freefall time and the time-scales for stellar evolution. Apart from this non-trivial rescaling, the time evolution of the dominant cluster is similar in the fiducial and the high surface density runs.

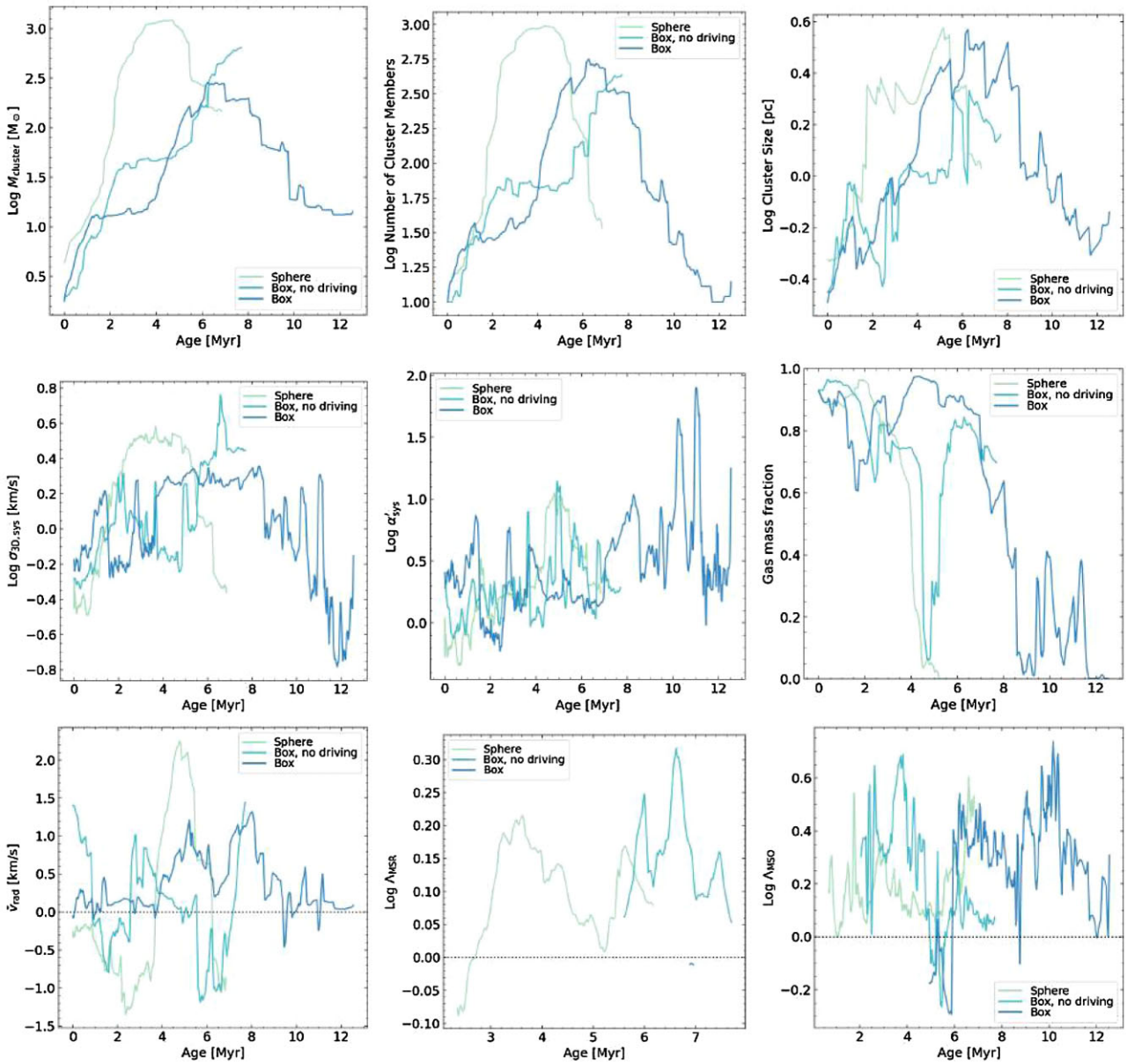

Figure 11. Evolution of the dominant cluster in a set of runs using both Sphere and Box, initial conditions for **M2e4** (see Table 1). The *top row* shows the total stellar mass in the cluster (left), number of cluster members (middle) and the cluster size scales (right, equation 1), respectively. The *middle row* shows the cluster velocity dispersion (left, equation 2), virialization state (middle, equation 4), and the gas mass fraction within the cluster radius (like Fig. 5 panel e). The *bottom row* shows the $\bar{v}_{rad}$ mass-weighted mean radial velocity for the cluster (left, equation 8), as well as the mass segregation ratio (right, equation 9) and mass segregation offset (right, equation 10). Note defining Λ_{MSR} requires a minimum of five massive stars to be in the cluster, while Λ_{MSO} requires only a single massive star. All values are smoothed with a 50 kyr averaging window to make the plots easier to read. For an analysis of the main trends, see Section 4.1 in the main text.

5 DISCUSSION

5.1 Cluster assembly and dynamical effects

Clusters in our simulations form through the mergers of accreting subclusters, which in turn merge to form ever larger structures, corresponding to a hierarchical assembly of clusters. This is similar to the behaviour found by recent simulations of larger ISM regions with lower mass resolution and a different subsets of the physics included in this work (Dobbs et al. 2022; Rieder et al. 2022). By the time, stellar feedback becomes important in the simulation most stars are concentrated in one or a few clusters. Stellar feedback eventually expels the remaining gas and the clusters become unbound, leading to their expansion and breakup (Tutukov 1978; Hills 1980; Mathieu 1983).

This qualitative picture appears to be robust to changes in initial conditions, such as turbulence or surface density, even though these simulations have significantly different star formation histories. We find that using periodic boundary conditions (Box runs) significantly hinders hierarchical cluster assembly, as it significantly decreases the overall gravitational potential (Federrath & Klessen 2012), weaken-

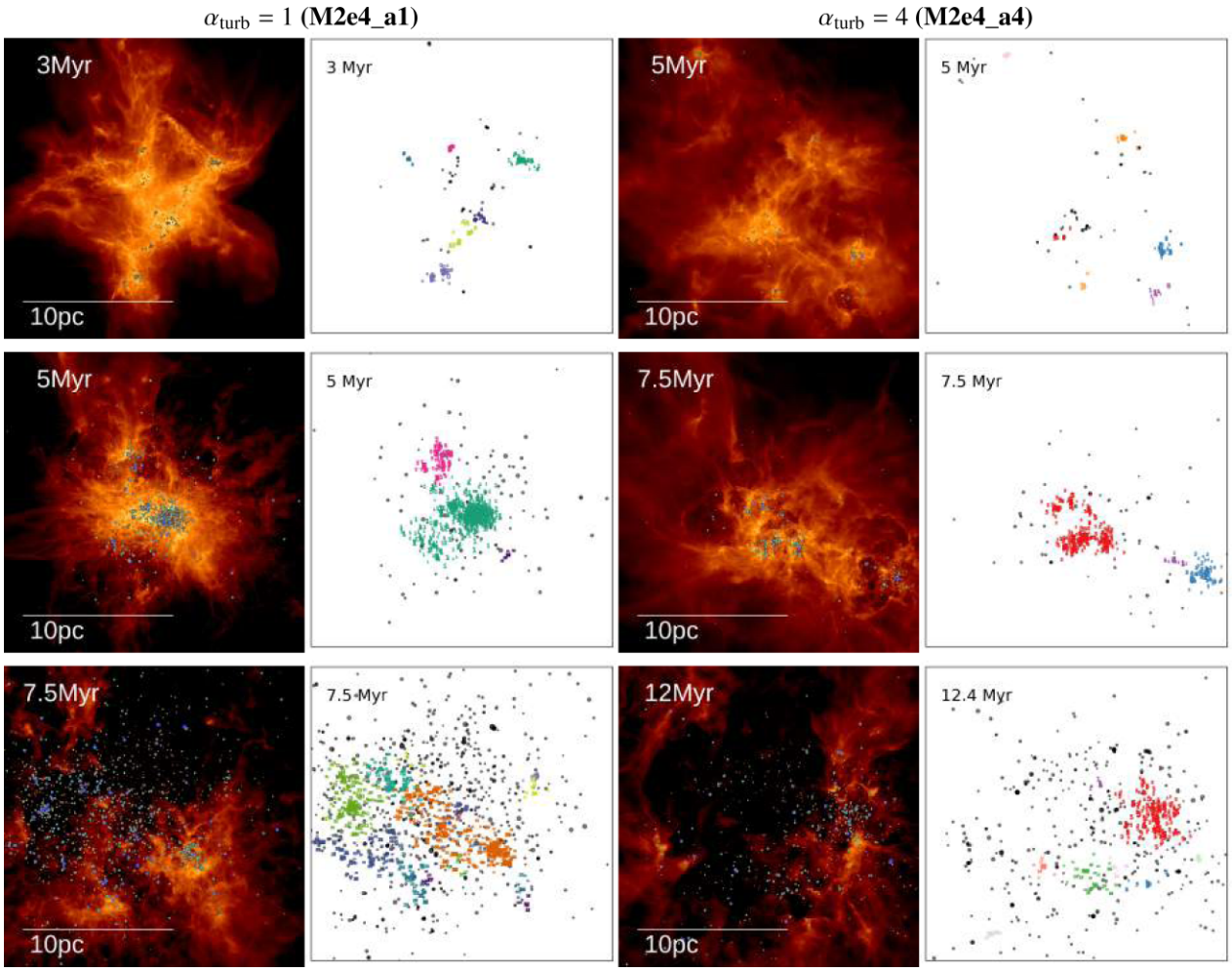

Figure 12. Same as Fig. 8 but for runs with initial turbulent virial parameters of $\alpha_{\rm turb} = 1$ and $\alpha_{\rm turb} = 4$ respectively (**M2e4_a1** and **M2e4_a4**).

ing gravitational focusing. In the Box run with external driving, we find that continued driving effectively prevents hierarchical merging. In this case, a significant fraction of newly formed clusters are transient and dissolve after <2 Myr (Fig. 10). We find that turbulent driving significantly increases the number of stars outside clusters (Table 2), making it one of the few parameters that can significantly affect clustering.

Recent observations found the high mass slope of the initial mass function in young clusters is steeper than the Milky Way average (Weisz et al. 2015). One possible explanation for the deficit of high mass stars is dynamical interactions that preferentially eject massive members (see Oh & Kroupa 2016). This is supported by recent observations finding a significant number of 'runaway' O and B stars ejected from young star clusters (Lennon et al. 2018; Zeidler et al. 2021). In our simulations we find no evidence that high-mass stars are preferentially ejected. Stars within clusters, outside clusters and ejected from clusters all appear to be drawn from the same underlying mass distribution. It should, however, be noted that the clusters in our simulations are actively accreting and gas-dominated, while previous work in the literature involved *N*-body simulations of gas-free, bound clusters. Since our simulations run only until gas expulsion occurs, our results neglect longer scale dynamical interactions, which could occur in the gas-free star clusters after star formation ceases.

5.2 Mass segregation

One key question of cluster formation is whether clusters form mass segregated or become so through dynamical interactions. In our simulations, star formation sites often host a single or several massive stars ($M_\star > 5\,{\rm M}_\odot$) at their centre, making them mass segregated (note that $\Lambda_{\rm MSR}$ is not defined for clusters with <5 massive stars). These small clusters merge to form larger structures, which in turn inherit the centrally condensed, mass-segregated substructures. Due to dynamical interactions these substructures strip stars from each other while merging. Over time dynamical processes cause the dense centres, which also host the massive stars, to sink to the centre of the larger merged structure. While these processes are taking place the substructures continue to grow, forming new stars as well as continuing to accrete gas. Thus we find that whether a cluster is considered mass-segregated depends greatly on the definitions of 'cluster' and 'mass segregation,' neither of which have one accepted definition in the literature (see Krumholz et al. 2019 for discussion). If one defines mass segregation as any stellar configuration where massive stars are distributed differently than lower mass stars (as in Krumholz et al. 2019), then star clusters start out mass segregation regardless of how cluster membership is assigned, since clusters contain substructures that host a single or a few massive stars at their respective centres. However, if mass segregation on the cluster scale occurs when massive stars are preferentially at the centre of the

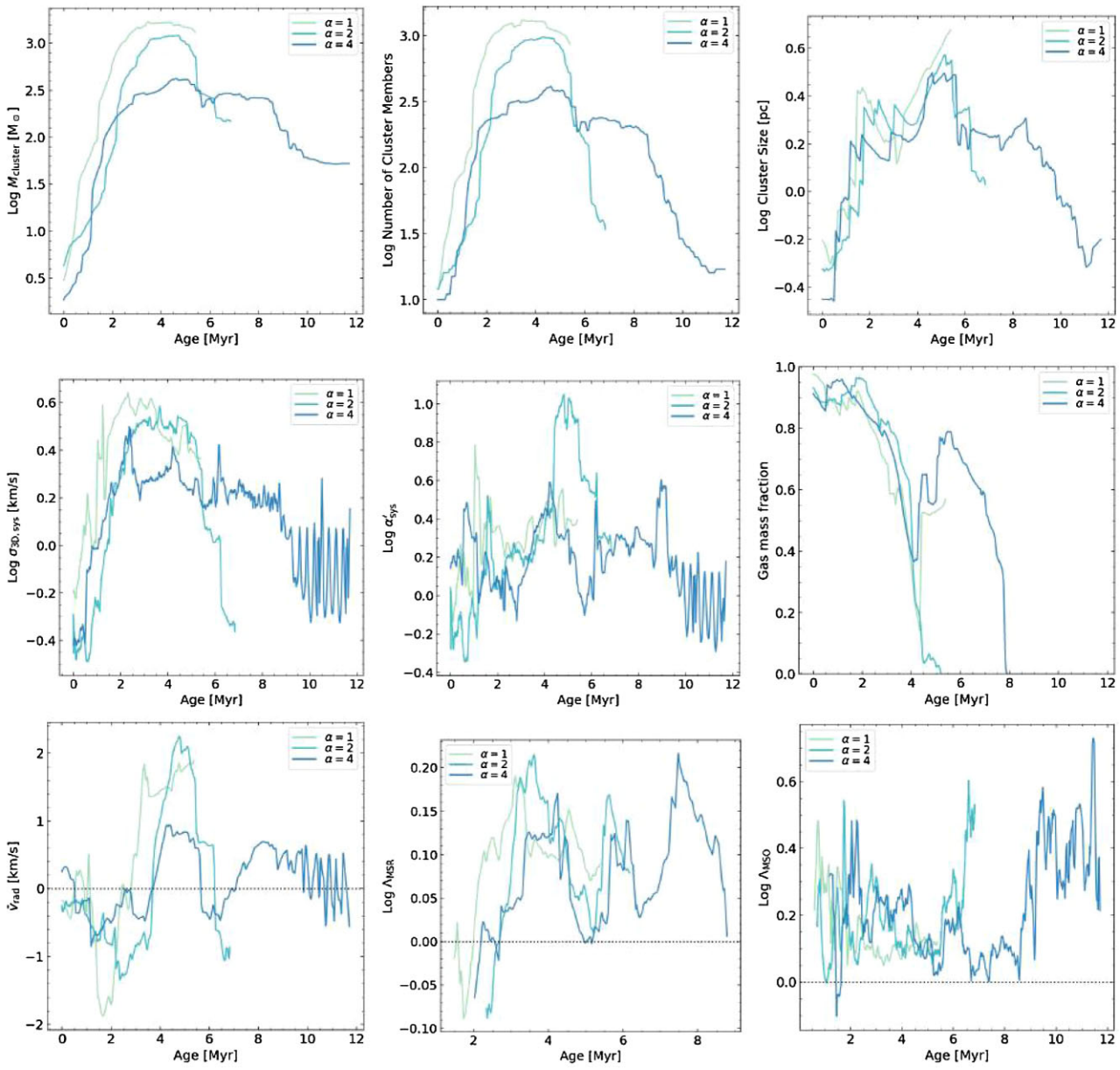

Figure 13. Evolution of the dominant cluster in a set of runs with different levels of initial turbulence (**M2e4_a1**, **M2e4**, and **M2e4_a4**, see Table 1), similar to Fig. 11. The *top row* shows the total stellar mass in the cluster (left), number of cluster members (middle), and the cluster size scales (right, equation 1), respectively. The *middle row* shows the cluster velocity dispersion (left, equation 2), virialization state (middle, equation 4), and the gas mass fraction within the cluster radius (like Fig. 5 panel e). The *bottom row* shows the $\bar{v}_{rad}$ mass-weighted mean radial velocity for the cluster (left, equation 8), as well as the mass segregation ratio (right, equation 9), and mass segregation offset (right, equation 10). For an analysis of the main trends see Section 4.2 in the main text.

cluster, as in de Grijs et al. (2002) and Krause et al. (2020), then the cluster definition determines whether the stars are mass segregated. Choosing a method that picks out structures containing several star formation sites (like the one we used) leads to no initial mass segregation (see the scenario in Fig. 2 and the evolution in Fig. 5). If, however, a cluster definition picks out individual star formation sites (e.g. by defining a smaller characteristic length or by requiring that a cluster be centrally condensed), then mass segregation will appear primordial regardless of metric (see Table 3 for a summary).

Most observers define clusters as pc-sized objects with many stars (Kirk & Myers 2011) and use mass segregation metrics that are insensitive to the mass segregation of any substructures within the cluster (e.g. de Grijs et al. 2002). In this framework, clusters in the simulation are initially not mass segregated and become so through dynamical interactions. The process takes several Myr, which is enough time for feedback from massive stars to expel gas but not enough time for the cluster to reach a fully relaxed state.

5.3 Caveats

While the simulations presented here represent the current state-of-the-art for simulating star-forming clouds, STARFORGE employs a large number of approximations and assumptions to make the simulations computationally tractable like other simulations in the literature (see Paper I for detailed discussions). In particular, there are significant caveats when applying STARFORGE to model star

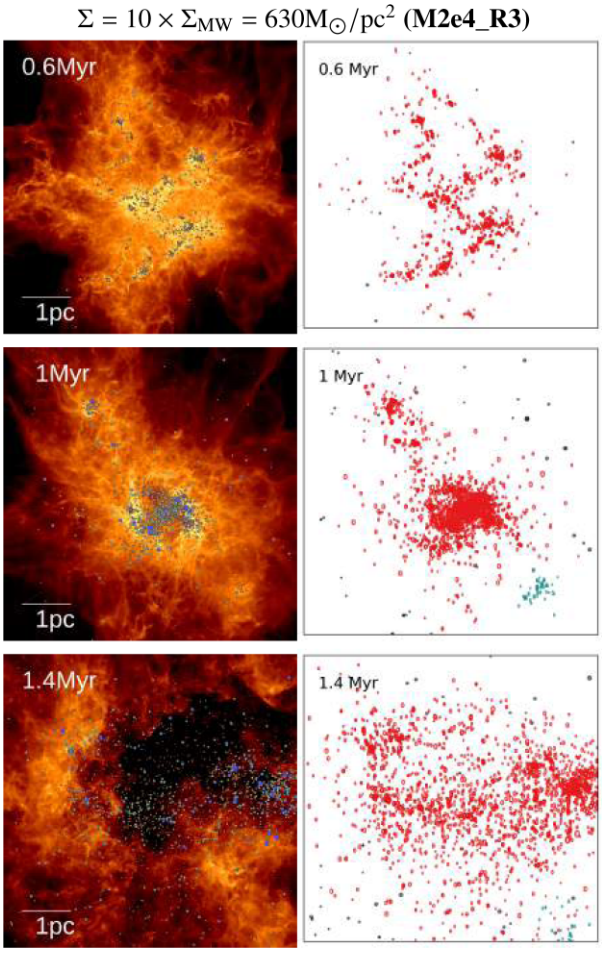

Figure 14. Same as Fig. 8 but for a run with 10 times higher initial surface density (**M2e4_R3**).

Table 3. Summary of our results regarding the initial mass segregation of newly formed clusters. We find that the answer depends on the definition of a cluster, i.e. whether the selected objects have substructure, and whether we define mass segregation as 'massive stars at the centre' (like Gouliermis et al. 2009) or as 'massive stars are distributed differently' (like Krumholz et al. 2019).

Cluster definition	Is there primordial mass segregation?	
	Massive stars at the centre	Distributed differently
No substructure	Y	Y
With substructure	N	Y

cluster formation. First, the runs have a ∼30 AU Jeans-resolution, i.e. fragmentation on scales smaller than this are not resolved. This resolution in the ideal-MHD limit effectively suppresses the formation of protostellar discs. Consequently, there is no disc fragmentation, causing the simulation to potentially miss closely formed binaries. The simulations presented here also use a gravitational softening length of ∼20 AU, making gravitational interactions below this scale inaccurate and suppressing the formation of binaries with separations smaller than this value. As a result, the long-term accuracy of *N*-body interactions is significantly lower than pure *N*-body simulations. It should be noted, however, that we run our simulations until gas expulsion, corresponding to a relatively short time after star formation starts (<5 Myr). Also, our clusters are gas-dominated for most of their lifetime and do not achieve high stellar densities, making close encounters rarer and lessening the effects of the gravitational softening on stellar interactions. Since, we terminate the simulations soon after cloud disruption, we cannot predict the ultimate fate of the clusters, bound mass fraction and cluster mass function. We will investigate the long-term evolution and fate of the STARFORGE clusters in a follow-up paper.

6 CONCLUSIONS

In this work, we analyse the star cluster assembly process in the STARFORGE radiation-magnetohydrodynamic simulations. These simulations follow the evolution of a mid-sized molecular cloud ($M = 20\,000\,M_\odot$, $\Sigma \sim 60\,M_\odot/pc^2$) taking into account gravity, gas thermodynamics, turbulence, magnetic fields, and radiation as well as stellar feedback processes (jets, radiation, winds, SNe).

Star clusters assemble through a series of mergers, whereby accreting star-formation sites come together to form larger structures. This hierarchical assembly continues until most stars end up in one or a few large, gas-dominated clusters. Once stellar feedback expels the gas they become unbound and the stars disperse. During the assembly process clusters eject a small fraction of their members (<10 per cent). We find no significant difference between the mass distribution of the ejected stellar population and that of the overall stellar mass spectrum of the simulation.

We investigate the effect of surface density and turbulence on the cluster formation process. We find that while the initial surface density and level of turbulence significantly affect the star formation history of the cloud, they do not qualitatively affect the cluster formation process.

We also investigate the effects of different initial cloud geometries and turbulent driving. We find that turbulent driving and a periodic 'Box' geometry significantly reduces clustering and suppresses cluster mergers. This is caused by weaker gravitational focusing, as periodic boundaries lead to a shallower gravitational potential, while maintaining turbulence reduces collapse.

We consider two different definitions for mass segregation. In all simulations, small forming groups of stars are initially mass segregated with one or a few massive stars at their centre. As these structures merge, they (at first) become mass-segregated substructures within the newly formed cluster. Thus, massive stars are not initially in the centre of merged clusters. Through dynamical interactions they relax to a centralized configuration, similar to that of observed clusters. We find that whether clusters are quantitatively considered to be mass segregated depends greatly on how one defines a cluster and mass segregation. If clusters are defined as structures that include many star-formation sites distributed throughout the GMC and mass segregation requires massive stars to be at the centre (both of these are true for most definitions used in observations), then there is no primordial mass segregation. Rather, mass segregation results from dynamical interactions. On the other hand, massive stars are usually centrally located within bound sub-groups of stars, such that they are distributed differently with respect to low-mass stars. Thus, a definition of mass segregation that does not require massive stars to be globally centralized, concludes that clusters start out mass segregated (see Table 3 for a summary).

In the simulations, dynamical evolution is still ongoing at the time of gas expulsion. Future work will investigate the evolution of the stellar distribution over 100 Myr time-scales and determine the survival rate of the star clusters we identify here.

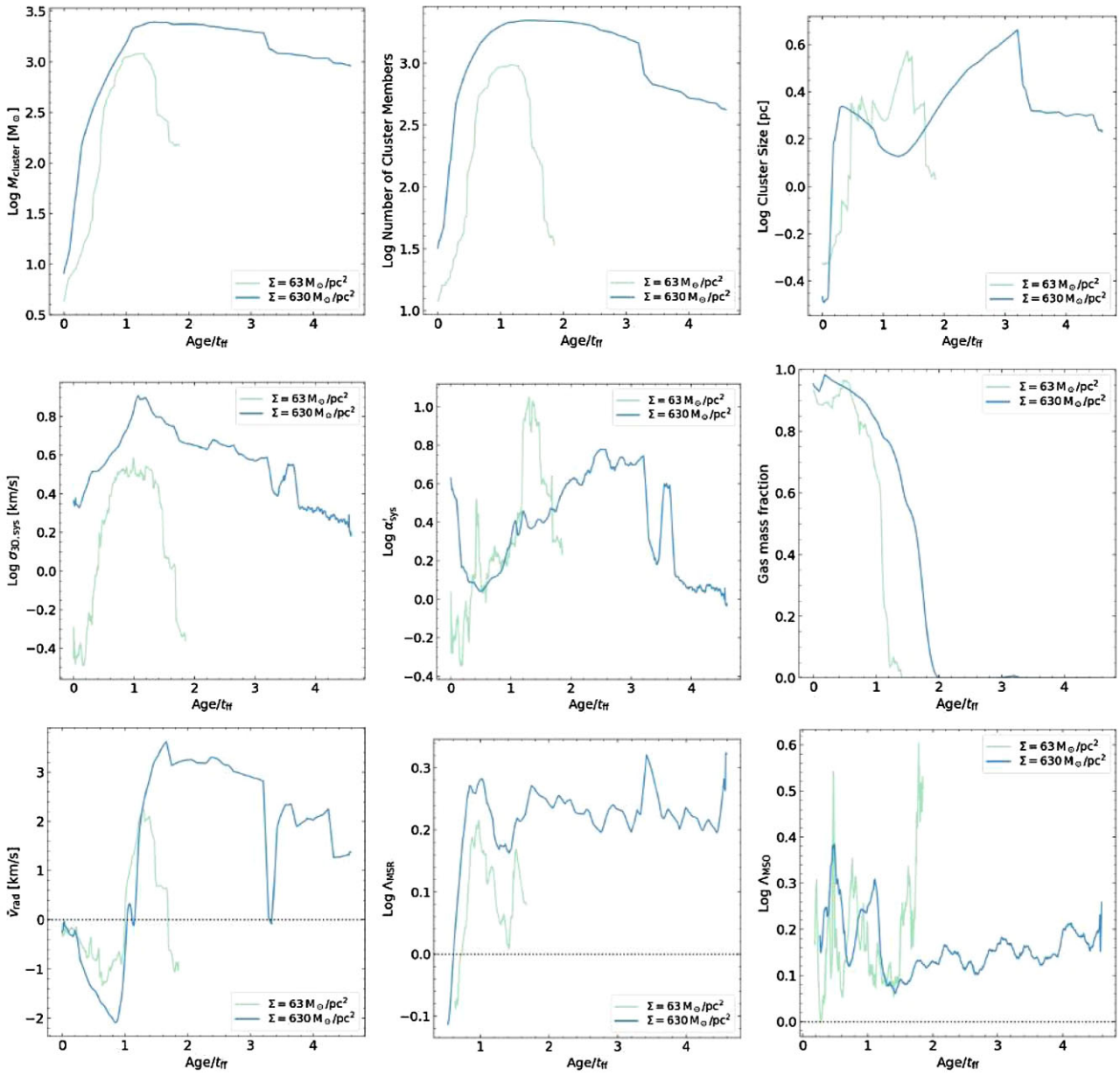

Figure 15. Evolution of the most dominant cluster in a set of runs with different initial surface densities (**M2e4** and **M2e4_R3**, see Table 1), similar to Fig. 11. To make the runs easier to compare, we normalized the time evolutions with the freefall times of the respective initial clouds (3.7 and 0.6 Myr for**M2e4** and **M2e4_R3,** respectively). The *top row* shows the total stellar mass in the cluster (left), number of cluster members (middle), and the cluster size scales (top right, equation 1), respectively. The *middle row* shows the cluster velocity dispersion (left, equation 2), virialization state (middle, equation 4), and the gas mass fraction within the cluster radius (like Fig. 5 panel e). The *bottom row* shows the $\bar{v}_{\rm rad}$ mass-weighted mean radial velocity for the cluster (left, equation 8), as well as the mass segregation ratio (right, equation 9), and mass segregation offset (right, equation 10). For an analysis of the main trends see Section 4.3 in the main text.

ACKNOWLEDGEMENTS

We would like to thank Sinan Deger for his thoughtful comments.

DG is supported by the Harlan J. Smith McDonald Observatory Postdoctoral Fellowship and the Cottrell Fellowships Award (#27982) from the Research Corporation for Science Advancement. Support for MYG was provided by NASA through the NASA Hubble Fellowship grant # HST-HF2-51479 awarded by the Space Telescope Science Institute, which is operated by the Association of Universities for Research in Astronomy, Inc., for NASA, under contract NAS5-26555. Support for PFH was provided by NSF Collaborative Research Grants 1715847 & 1911233, NSF CAREER grant 1455342, and NASA grants 80NSSC18K0562 & JPL 1589742. SSRO and CM are supported by NSF Career Award AST-1748571 and by a Cottrell Scholar Award from the Research Corporation for Science Advancement. CAFG was supported by NSF through grants AST-1715216, AST-2108230, and CAREER award AST-1652522; by NASA through grant 17-ATP17-0067; by STScI through grant HST-AR-16124.001-A; and by the Research Corporation for Science Advancement through a Cottrell Scholar Award. ALR acknowledges support from Harvard University through the ITC Post-doctoral Fellowship. This work used computational resources provided by XSEDE allocation AST-190018, the Frontera allocation AST-20019, and additional resources provided by the University of Texas at

Austin and the Texas Advanced Computing Center (TACC; http://www.tacc.utexas.edu).

DATA AVAILABILITY

The data supporting the plots within this article are available on reasonable request to the corresponding authors. A public version of the GIZMO code is available at http://www.tapir.caltech.edu/~phopkins/Site/GIZMO.html.

REFERENCES

Allison R. J., Goodwin S. P., Parker R. J., Portegies Zwart S. F., de Grijs R., Kouwenhoven M. B. N., 2009, MNRAS, 395, 1449
Attias H., 2000, Adv. Neural Inf. Process. Syst., 12, 209
Bate M. R., 2009, MNRAS, 392, 1363
Bate M. R., Bonnell I. A., Price N. M., 1995, MNRAS, 277, 362
Bauer A., Springel V., 2012, MNRAS, 423, 2558
Baumgardt H., Kroupa P., 2007, MNRAS, 380, 1589
Behroozi P. S., Wechsler R. H., Wu H.-Y., 2013, ApJ, 762, 109
Binney J., Tremaine S., 1987, Galactic dynamics, 2nd edn. Princeton University Press, Princeton
Bishop C. M., 2006, Pattern Recognition and Machine Learning. Springer, New York
Bonnell I., Bate M., 2006, MNRAS, 370, 488
Bonnell I. A., Bate M. R., Vine S. G., 2003, MNRAS, 343, 413
Bressert E. et al., 2010, MNRAS, 409, L54
Cartwright A., Whitworth A. P., 2004, MNRAS, 348, 589
Cunningham A. J., Krumholz M. R., McKee C. F., Klein R. I., 2018, MNRAS, 476, 771
de Grijs R., Gilmore G. F., Johnson R. A., Mackey A. D., 2002, MNRAS, 331, 245
Dobbs C. L., Bending T. J. R., Pettitt A. R., Bate M. R., 2022, MNRAS, 509, 954
Draine B. T., 2011, Physics of the Interstellar and Intergalactic Medium, Princeton University Press, Princeton
Ester M., Kriegel H.-P., Sander J., Xu X. 1996, in Kdd. AAAI Press, p. 226
Fall S. M., Krumholz M. R., Matzner C. D., 2010, ApJ, 710, L142
Farias J. P., Fellhauer M., Smith R., Domínguez R., Dabringhausen J., 2018, MNRAS, 476, 5341
Federrath C., Klessen R. S., 2012, ApJ, 761, 156
Federrath C., Roman-Duval J., Klessen R. S., Schmidt W., Mac Low M.-M., 2010, A&A, 512, A81
Federrath C., Schrön M., Banerjee R., Klessen R. S., 2014a, ApJ, 790, 128
Federrath C., Schober J., Bovino S., Schleicher D. R. G., 2014b, ApJ, 797, L19
Ferland G. J. et al., 2013, RMxAA, 49, 137
Foster J. B. et al., 2015, ApJ, 799, 136
Geen S., Watson S. K., Rosdahl J., Bieri R., Klessen R. S., Hennebelle P., 2018, MNRAS, 481, 2548
Gieles M., Sana H., Portegies Zwart S. F., 2010, MNRAS, 402, 1750
Gouliermis D. A., 2018, PASP, 130, 072001
Gouliermis D., Keller S. C., Kontizas M., Kontizas E., Bellas-Velidis I., 2004, A&A, 416, 137
Gouliermis D. A., de Grijs R., Xin Y., 2009, ApJ, 692, 1678
Grudic M. Y., Guszejnov D., 2021, MakeCloud, available at https://github.com/mikegrudic/MakeCloud
Grudić M. Y., Guszejnov D., Hopkins P. F., Lamberts A., Boylan-Kolchin M., Murray N., Schmitz D., 2018, MNRAS, 481, 688
Grudić M. Y., Guszejnov D., Hopkins P. F., Offner S. S. R., Faucher-Giguère C.-A., 2021a, MNRAS, 506, 2199 (Paper I)
Grudić M. Y., Kruijssen J. M. D., Faucher-Giguère C.-A., Hopkins P. F., Ma X., Quataert E., Boylan-Kolchin M., 2021b, MNRAS, 506, 3239
Grudić M. Y., Guszejnov D., Offner S. S. R., Rosen A. L., Raju A. N., Faucher-Giguère C.-A., Hopkins P. F., 2022, MNRAS, 512, 216
Guszejnov D., Hopkins P. F., Krumholz M. R., 2017, MNRAS, 468, 4093
Guszejnov D., Grudić M. Y., Hopkins P. F., Offner S. S. R., Faucher-Giguère C.-A., 2020, MNRAS, 496, 5072
Guszejnov D., Grudić M. Y., Hopkins P. F., Offner S. S. R., Faucher-Giguère C.-A., 2021, MNRAS, 502, 3646 (Paper II)
Hillenbrand L. A., 1997, AJ, 113, 1733
Hillenbrand L. A., Hartmann L. W., 1998, ApJ, 492, 540
Hills J. G., 1980, ApJ, 235, 986
Hopkins P. F., 2015, MNRAS, 450, 53
Hopkins P. F., 2016, MNRAS, 462, 576
Hopkins P. F., Raives M. J., 2016, MNRAS, 455, 51
Hopkins P. F. et al., 2018, MNRAS, 480, 800
Hopkins P. F., Grudić M. Y., Wetzel A., Kereš D., Faucher-Giguère C.-A., Ma X., Murray N., Butcher N., 2020, MNRAS, 491, 3702
Kerr R. M. P., Rizzuto A. C., Kraus A. L., Offner S. S. R., 2021, ApJ, 917, 23
Kirk H., Myers P. C., 2011, ApJ, 727, 64
Kirk H., Offner S. S. R., Redmond K. J., 2014, MNRAS, 439, 1765
Krause M. G. H. et al., 2020, Space Sci. Rev., 216, 64
Kroupa P., 2002, Science, 295, 82
Kruijssen J. M. D., 2014, Class. Quantum Gravity, 31, 244006
Krumholz M. R., McKee C. F., 2008, Nature, 451, 1082
Krumholz M. R., McKee C. F., 2020, MNRAS, 494, 624
Krumholz M. R., McKee C. F., Bland-Hawthorn J., 2019, ARA&A, 57, 227
Kuhn M. A. et al., 2014, ApJ, 787, 107
Kuhn M. A., Hillenbrand L. A., Sills A., Feigelson E. D., Getman K. V., 2019, ApJ, 870, 32
Lada C. J., Dame T. M., 2020, ApJ, 898, 3
Lada C. J., Lada E. A., 2003, ARA&A, 41, 57
Lamers H. J. G. L. M., Snow T. P., Lindholm D. M., 1995, ApJ, 455, 269
Larson R. B., 1981, MNRAS, 194, 809
Lennon D. J. et al., 2018, A&A, 619, A78
Levermore C. D., 1984, J. Quant. Spec. Radiat. Transf., 31, 149
Li P. S., Norman M. L., Mac Low M.-M., Heitsch F., 2004, ApJ, 605, 800
Mathieu R. D., 1983, ApJ, 267, L97
McInnes L., Healy J., Astels S., 2017, J. Open Source Softw., 2, 205
McKee C. F., Tan J. C., 2003, ApJ, 585, 850
McKee C. F., Parravano A., Hollenbach D. J., 2015, ApJ, 814, 13
Meynet G., Maeder A., 2005, A&A, 429, 581
Mouschovias T. C., Spitzer L. J., 1976, ApJ, 210, 326
Offner S. S. R., Klein R. I., McKee C. F., Krumholz M. R., 2009a, ApJ, 703, 131
Offner S. S. R., Hansen C. E., Krumholz M. R., 2009b, ApJ, 704, L124
Oh S., Kroupa P., 2016, A&A, 590, A107
Ostriker E. C., Stone J. M., Gammie C. F., 2001, ApJ, 546, 980
Parker R. J., 2014, MNRAS, 445, 4037
Pedregosa F. et al., 2011, J. Mach. Learn. Res., 12, 2825
Portegies Zwart S. F., McMillan S. L. W., Gieles M., 2010, ARA&A, 48, 431
Price D. J., Monaghan J. J., 2007, MNRAS, 374, 1347
Rieder S., Dobbs C., Bending T., Liow K. Y., Wurster J., 2022, MNRAS, 509, 6155
Schmeja S., 2011, Astron. Nachr., 332, 172
Smith N., 2014, ARA&A, 52, 487
Spitzer, Lyman J., 1969, ApJ, 158, L139
Spitzer, Lyman J., Harm R., 1958, ApJ, 127, 544
Springel V., 2005, MNRAS, 364, 1105
Tutukov A. V., 1978, A&A, 70, 57
Vaidya B., Mignone A., Bodo G., Massaglia S., 2015, A&A, 580, A110
Vázquez-Semadeni E., González-Samaniego A., Colín P., 2017, MNRAS, 467, 1313
Wall J. E., Mac Low M.-M., McMillan S. L. W., Klessen R. S., Portegies Zwart S., Pellegrino A., 2020, ApJ, 904, 192
Weisz D. R. et al., 2015, ApJ, 806, 198
Wiersma R. P. C., Schaye J., Smith B. D., 2009, MNRAS, 393, 99
Zamora-Avilés M., Ballesteros-Paredes J., Hernández J., Román-Zúñiga C., Lora V., Kounkel M., 2019, MNRAS, 488, 3406
Zeidler P., Sabbi E., Nota A., McLeod A. F., 2021, AJ, 161, 140

This paper has been typeset from a TEX/LATEX file prepared by the author.